



Buckyball-metal Complexes as Potential Carriers of Astronomical Unidentified Infrared Emission Bands

Gao-Lei Hou^{5,1} , Olga V. Lushchikova² , Joost M. Bakker² , Peter Lievens¹ , Leen Decin^{3,4} , and Ewald Janssens¹

¹ Quantum Solid-State Physics, KU Leuven, Celestijnenlaan 200D, B-3001 Leuven, Belgium

² Radboud University, Institute for Molecules and Materials, FELIX Laboratory, Toernooiveld 7, 6525 ED Nijmegen, The Netherlands

³ Institute of Astronomy, KU Leuven, Celestijnenlaan 200D, B-3001 Leuven, Belgium; leen.decin@kuleuven.be

⁴ School of Chemistry, University of Leeds, Leeds, LS2 9JT, UK

⁵ MOE Key Laboratory for Non-Equilibrium Synthesis and Modulation of Condensed Matter, School of Physics, Xi'an Jiaotong University, Xi'an, 710049 Shaanxi, People's Republic of China; gaolei.hou@xjtu.edu.cn

Received 2023 January 24; revised 2023 April 13; accepted 2023 April 18; published 2023 July 14

Abstract

Efforts over 40 yr still leave the source of astronomical infrared emission bands largely unidentified. Here, we report the first laboratory infrared (6–25 μm) spectra of gas-phase fullerene-metal complexes, $[\text{C}_{60}\text{-Metal}]^+$ (Metal = Fe, V) and show with density functional theory calculations that complexes of C_{60} with cosmically abundant metals, including Li, Na, K, Mg, Ca, Al, V, and Fe, all have similar spectral patterns. Comparison with observational infrared spectra from several fullerene-rich planetary nebulae demonstrates a strong positive linear cross-correlation. The infrared features of $[\text{C}_{60}\text{-Metal}]^+$ coincide with four bands attributed earlier to neutral C_{60} bands and in addition also with several bands unexplained to date. Abundance and collision theory estimates indicate that $[\text{C}_{60}\text{-Metal}]^+$ could plausibly form and survive in astrophysical environments. Hence, $[\text{C}_{60}\text{-Metal}]^+$ are proposed as promising carriers, in supplement to C_{60} , of observational bands, potentially representing the largest molecular species in space other than C_{60} , C_{60}^+ , and C_{70} .

Unified Astronomy Thesaurus concepts: Laboratory astrophysics (2004); Experimental techniques (2078); Molecular physics (2058)

1. Introduction

Astronomical unidentified infrared emission (UIE) bands with wavelengths between 3 and 20 μm are observed in a variety of astrophysical environments (Leger & Puget 1984; Boersma et al. 2014). They were discovered in the 1970s and are generally attributed to organic compounds in cosmic environments (Knacke 1977; Russell et al. 1977). They contain a wealth of information about the physical and chemical conditions in the emitting regions, but their precise carriers are largely unknown, knowledge of which is potentially crucial to probe cosmic star formation history, interstellar chemistry, and galactic evolution (Tielens 2008; Kwok & Zhang 2011; Kwok 2017).

Over the past 40 yr, general consensus has been reached that UIE features at 3.3, 6.2, 7.7, 8.6, and 11.3 μm can be attributed predominantly to vibrations of polycyclic aromatic hydrocarbon (PAH) molecules, although the exact nature of the emitting PAHs remains elusive (Salama 2008; Tielens 2008; Kwok & Zhang 2011, 2013; Tielens 2013; Kwok 2017; Candian et al. 2018). Later, an alternative model based on mixed aromatic/aliphatic organic nanoparticles (MAON) from the observation of spectral features at 3.4 and 6.85 μm , characteristic of aliphatic compounds, was proposed (Kwok & Zhang 2011). Still, both the PAH hypothesis and the MAON model are under discussion (Li & Draine 2012; Kwok & Zhang 2013; Kwok 2017).

In contrast, fullerenes have been confirmed unequivocally as UIE carriers (Cami et al. 2010; García-Hernández et al. 2010;

Sellgren et al. 2010; García-Hernández et al. 2011; Bernard-Salas et al. 2012; Berné et al. 2013; Otsuka et al. 2016), notably in the young planetary nebula (PN) Tc 1, in particular through the C_{60} infrared spectral signatures at 7.0, 8.5, 17.4, and 18.9 μm (Cami et al. 2010). Its cation, C_{60}^+ , was speculated to be present in the reflection nebula NGC 7023 from bands at 6.4, 7.1, 8.2, and 10.5 μm (Berné et al. 2013) before it was firmly identified, through laboratory measurement, as a carrier of diffuse interstellar bands (DIBs) at 9577 and 9632 Å (Campbell et al. 2015; Maier & Campbell 2017; Cordiner et al. 2019). To date, C_{60} and C_{60}^+ have been detected in more than 40 cosmic environments (Woods 2020). Four planetary nebulae (PNe), Tc 1, SMP LMC 56, SMP SMC 16, and Lin 49, are particularly interesting, as their UIE bands show they are C_{60} -rich with almost no infrared emissions at wavelengths characteristic for PAHs (Cami et al. 2010; Bernard-Salas et al. 2012; Berné et al. 2013; Otsuka et al. 2016).

Although the presence of C_{60} in space is nowadays unambiguous, current knowledge is incomplete as neither fluorescence nor thermal excitation mechanisms can explain the observed band intensity ratios of the four C_{60} features, while the carriers of many other UIE features remain unknown (Cami et al. 2010; Bernard-Salas et al. 2012; Berné et al. 2013; Otsuka et al. 2016; Woods 2020; Kwok 2022). One possible source could be fullerene complexes with other astronomically abundant species. Already shortly after its discovery in 1985 (Kroto et al. 1985), the exceptional stability of C_{60} led Kroto to speculate on its relevance to unidentified interstellar spectroscopic features, including the potential presence of exohedral charge-transfer complexes of fullerenes with cosmically abundant metals, $[\text{C}_{60}\text{-Metal}]^+$ (Kroto 1988; Kroto & Jura 1992; Omont 2016). The metal atom will break the icosahedral symmetry of C_{60} and the expected strong C_{60} -metal interactions



Original content from this work may be used under the terms of the [Creative Commons Attribution 4.0 licence](#). Any further distribution of this work must maintain attribution to the author(s) and the title of the work, journal citation and DOI.

will affect the vibronic energy levels, introducing many active vibrational modes, similar to those recently reported for $C_{60}H^+$ (Palotás et al. 2020), as well as a wealth of electronic transitions. However, due to a lack of accurate gas-phase spectroscopic data, no observational confirmation of $[C_{60}\text{-Metal}]^+$ complexes in space has been reported (Omont 2016; Woods 2020).

2. Brief of Methods

2.1. Experimental

The $[C_{60}\text{-Metal}]^+$ (Metal = Fe and V) complexes are synthesized in vacuum by a dual-target dual-laser ablation source, which is a modified version of the Smalley-type laser vaporization source used in the discovery of C_{60} in 1985 (Kroto et al. 1985) and has been described in detail previously (Ferrari et al. 2017). Infrared multiple photon dissociation (IRMPD) experiments are performed by overlapping the shaped cluster beam with IR light of the Free Electron Laser for Intra-Cavity Experiments, FELICE (Bakker et al. 2010).

2.2. Theoretical

All calculations were conducted with the Gaussian 09 program package (Frisch et al. 2013).

2.3. Details on the Astronomical Data and the Cross-correlation Analysis

The Spitzer infrared spectra of Tc 1, LMC 56 and SMC 16, and Lin 49 are adapted from Cami et al. (2010), Bernard-Salas et al. (2012), and Otsuka et al. (2016). The similarity between each of the four Spitzer PN spectra and laboratory infrared spectra is quantified by the cross-correlation coefficient, which is a preferred and well-established method of choice for the analysis of one component in a complex system (Koenig 1999).

Further details are provided in the Appendix.

3. Results

We developed an experimental protocol to measure, for the first time, the laboratory infrared ($6\text{--}25\ \mu\text{m}$) spectra of $[C_{60}\text{-Metal}]^+$ (Metal = Fe and V) complexes via messenger-tagged IRMPD spectroscopy, in which either an argon atom or a D_2 molecule serves as a weakly bound spectator to probe the absorption of infrared light by $[C_{60}\text{-Metal}]^+$ (see the Experimental section of the Appendix). Figure 1(a) shows the mass distributions of $C_{60}\text{Fe}^+$ and its Ar-tagged complexes with (red) and without (black) infrared irradiation at $515\ \text{cm}^{-1}$ ($19.4\ \mu\text{m}$). The carbon and iron isotope distributions can readily be recognized.

Figure 1(b) presents the laboratory IRMPD spectrum of Ar-tagged $C_{60}\text{Fe}^+$. Apart from four features coinciding with the C_{60} bands (indicated by the vertical red dotted lines), many more vibrational bands are visible. Figure 1(c) shows the theoretically simulated infrared spectrum of $C_{60}\text{Fe}^+$ using density functional theory (DFT) calculations (see the Theoretical section of the Appendix). The calculations essentially reproduce all observed infrared features, except that some intensities are slightly off. Such minor discrepancies are common when comparing DFT calculations with IRMPD experiments, where the multiple photon excitation process may cause deviations from the calculated linear absorption intensities (Calvo et al. 2015; Palotás et al. 2020). The overlap of the experimental infrared spectral features of C_{60} and

$C_{60}\text{Fe}^+$ may be due to the almost neutral character of C_{60} in $C_{60}\text{Fe}^+$, as our calculations show C_{60} carries only $+0.125\ e$ charge from natural population analysis. In Figure A1, the laboratory IRMPD spectrum of D_2 -tagged $C_{60}\text{V}^+$ and its comparison with both DFT calculations and that of $C_{60}\text{Fe}^+$ is provided, indicating that the spectral patterns of $C_{60}\text{V}^+$ and $C_{60}\text{Fe}^+$ have similar characteristic features (see detailed band positions in Table 1). Figure A2 overlays the calculated spectra of $C_{60}\text{V}^+$ with and without D_2 and of $C_{60}\text{Fe}^+$ with and without Ar. It can be seen that tags have little effect on the band positions especially in the case of $C_{60}\text{Fe}^+$, using Ar as a tag. In the case of $C_{60}\text{V}^+$, using D_2 as a tag, the appearance of new features around 540 and $810\ \text{cm}^{-1}$ is due to D_2 (see Figure A1).

The overall agreement between the theoretical and laboratory spectra of both $C_{60}\text{Fe}^+$ and $C_{60}\text{V}^+$ provides confidence that we can reliably predict the infrared spectra of C_{60} complexes with other cosmically abundant metals, such as Li, Na, K, Mg, Ca, and Al (Omont 2016). Calculations show they all have infrared spectral patterns similar to those of $C_{60}\text{Fe}^+$ or $C_{60}\text{V}^+$ (Figure A3). Vibrational analysis indicates that most features involve motions of the C_{60} cage, perturbed by attaching metal atoms. Hence, the laboratory spectrum of either $C_{60}\text{Fe}^+$ or $C_{60}\text{V}^+$ can be considered as a model for various $[C_{60}\text{-Metal}]^+$ complexes.

To assess the plausibility of $[C_{60}\text{-Metal}]^+$ surviving under interstellar conditions, we used collision theory and the estimated 1% of cosmic carbon locked in C_{60} for evolved stars (Table A1) (Omont 2016; Woods 2020). With an assumed hydrogen number density of $2\times 10^4\ \text{cm}^{-3}$, $[C_{60}\text{-Metal}]^+$ formation rates are estimated to be, depending on the specific metal, in the range of $1\times 10^{-7}\text{--}4\times 10^{-2}\ \text{yr}^{-1}$ (C_{60} has a lifetime exceeding $10^8\ \text{yr}$ in space; see Table A2 and Omont 2016). The thermal dissociation rates of $[C_{60}\text{-Metal}]^+$ complexes at typical temperatures below $300\ \text{K}$ depend on their stabilities and are, for $C_{60}\text{V}^+$ and $C_{60}\text{Fe}^+$ with binding energies of 2.82 and $2.25\ \text{eV}$, respectively, significantly smaller than the formation rates (Table A2). The strong dependence of photodissociation on the ultraviolet radiation field and optical depth and its competition with radiative decay (via visible to infrared photon emission) and photoionization to higher charge states make an accurate estimate of the photodissociation rate challenging (see the Photodissociation Rates section of the Appendix). However, our analysis still indicates that $[C_{60}\text{-Metal}]^+$ could plausibly form and survive in certain astrophysical environments.

Our laboratory infrared spectra can be used to discuss the potential spectral impact of the presence of $[C_{60}\text{-Metal}]^+$ in space. The coexistence of different $[C_{60}\text{-Metal}]^+$ complexes in the same object will slightly modify the band positions and intensities (Table 1 and Figure A3). Figures 2(e)–(f) show the similarities between the laboratory $C_{60}\text{Fe}^+$ spectrum and a summed theoretical spectrum of $[C_{60}\text{-Metal}]^+$. The band shift at $18.9\ \mu\text{m}$ is due to an underestimation of that mode frequency by DFT calculations, also seen in calculations for neutral C_{60} (blue dashed lines in Figure 2(f); see also Figure A1). The overall agreement in band positions confirms that the laboratory spectra can serve as faithful models for various $[C_{60}\text{-Metal}]^+$ complexes.

Figures 2(a)–(d) display the continuum-subtracted Spitzer infrared spectra of Tc 1, LMC 56, SMC 16, and Lin 49 (Cami et al. 2010; Bernard-Salas et al. 2012; Otsuka et al. 2016), with observational and laboratory band positions summarized in Table 1. Note that to ease the comparison, all the Spitzer data have been rebinned to the wavelength grid of SMC 16 using

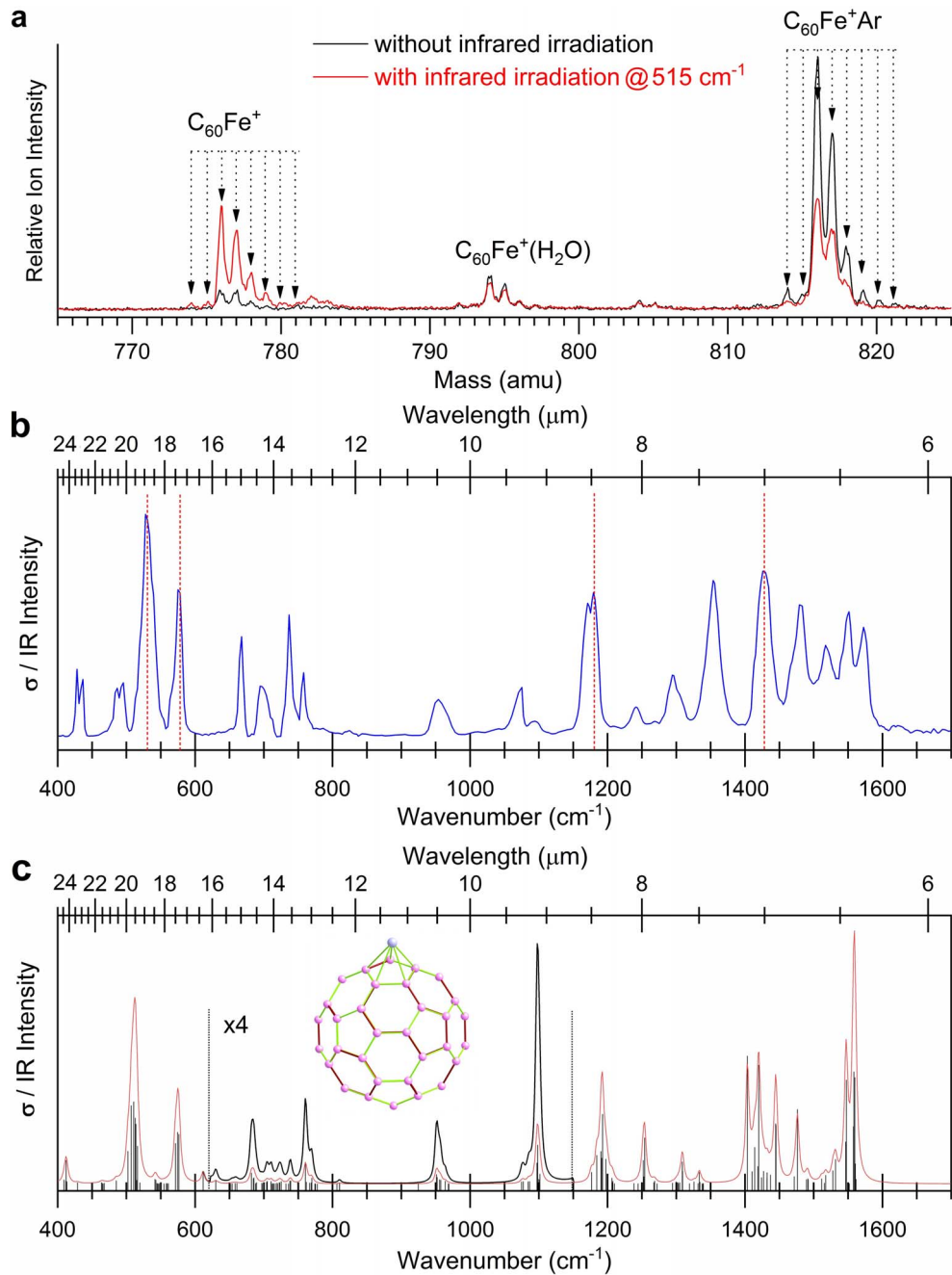


Figure 1. Laboratory synthesis and infrared spectroscopy of $C_{60}Fe^+$. (a) Mass distributions of $C_{60}Fe^+$ and its Ar-tagged complexes synthesized using a dual-target dual-laser vaporization source, with (red) and without (black) the infrared irradiation at 515 cm^{-1} . (b) IRMPD spectrum of Ar-tagged $C_{60}Fe^+$ in the $400\text{--}1700\text{ cm}^{-1}$ range. The positions of four neutral C_{60} bands are indicated with vertical red dotted lines. (c) Theoretically simulated spectrum of $C_{60}Fe^+$ at the BPW91/6-31G(d) level (red curve) with its calculated structure shown as an inset. The calculated intensities are plotted with sticks and convolved using Lorentzian line shapes of 6 cm^{-1} FWHM. The convolved spectrum is enlarged by a factor of 4 between $650\text{--}1150\text{ cm}^{-1}$ (black curve).

linear interpolation, which may smear out a few sharp atomic lines, in particular for the high-resolution spectral region ($9.8\text{--}19.5\text{ }\mu\text{m}$) of the Spitzer data of Tc 1 (Cami et al. 2010; see Details on the Astronomical Data section of the Appendix), but it will not affect the following analysis. The four characteristic features of neutral C_{60} (vertical blue dashed lines) are clearly seen in all four PNe, but with varying intensity ratios, and are also observed in the laboratory infrared spectra of $C_{60}Fe^+$ and $C_{60}V^+$ within the experimental and observational uncertainty. The spread in intensity ratios was also reported in many other C_{60} -containing astrophysical

environments (García-Hernández et al. 2011; Bernard-Salas et al. 2012; Otsuka et al. 2016; Zhang et al. 2017). It has been noted that the 17.4 and $18.9\text{ }\mu\text{m}$ features of LMC 56, SMC 16, and Lin 49 have small shoulders at longer wavelengths, for example, shoulders at about 17.8 and $18.1\text{ }\mu\text{m}$, and 20.2 and $20.6\text{ }\mu\text{m}$, as well as asymmetric band profiles (García-Hernández et al. 2011; Bernard-Salas et al. 2012; Otsuka et al. 2016). Such characteristics could indicate the presence of other contributing emitters (Bernard-Salas et al. 2012), as recently proposed from two laboratory bands of $C_{60}H^+$ at 17.7 and $19.1\text{ }\mu\text{m}$ (Palotás et al. 2020).

Table 1

The Infrared Spectral Band Positions from the Laboratory Experiment, the Calculation of the Most Stable $C_{60}V^+$, and the Spitzer Infrared Spectra of Tc 1, LMC 56, SMC 6, and Lin 49, as well as of C_{60} and C_{60}^+

Table 1
(Continued)

$C_{60}V^+$		$C_{60}Fe^+$	C_{60}	Tc 1 ^a	LMC 56 ^b	SMC 16 ^b	Lin 49 ^c	C_{60}^+ ^d	C_{60} gas (~ 1065 K) ^e	solid (~ 300 K) ^f	C_{70}	Atomic lines ^{a,b}
Lab. (cm $^{-1}$ /μm)	Theo. (cm $^{-1}$)	Lab. (cm $^{-1}$ /μm)	Theo. (cm $^{-1}$ /μm)	(μm)	(μm)	(μm)	(μm)	(μm)	(cm $^{-1}$ /μm)	(cm $^{-1}$ /μm)	Tc 1 ^a (μm)	(μm)
1426/7.01	1426	1427/7.00	1440/6.95	7.03	7.02	7.02	7.04		1406.9/7.11	1429/7.00		7.03 [Ar II]
1465/6.83	1440	1467/6.82					6.82					
1496/6.68	1485	1480/6.74		6.67	6.65							
1520/6.58	1514	1518/6.59				6.58	6.59					
	1531											
1550/6.45	1542	1550/6.45		6.48	6.47			6.4				6.48 [H_re]
1570/6.37	1562	1572/6.35		6.23	6.23							

Notes. The asterisks indicate the D₂-tag-induced features. Note that the small band position differences between the laboratory measurement and the astronomical observations can well be accounted for by considering the wavelength uncertainties in both laboratory and Spitzer data. For instance, even for the four neutral C₆₀ bands, there is about a 1% deviation of the band positions as seen in Tc 1.

^a From Cami et al. (2010)

^b From García-Hernández et al. (2011)

^c Otsuka, M. et al. (2016)

^d From Berné et al. (2013)

^e From Nemes et al. (1994)

^f From Krätschmer (1990).

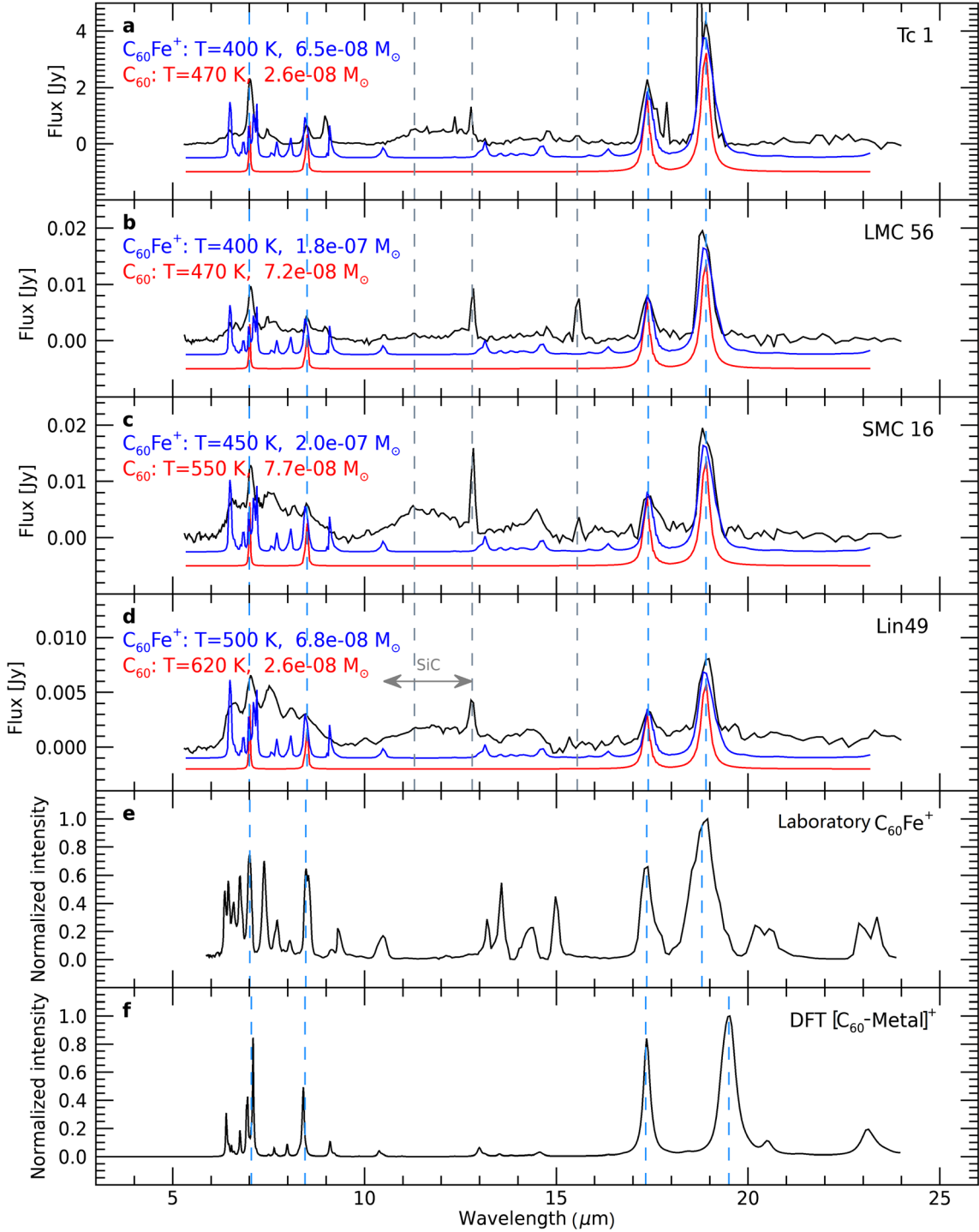


Figure 2. Comparison between the Spitzer infrared spectra of four fullerene-rich PNe (black) and the thermal emission model for C_{60} (red) and $C_{60}Fe^+$ (blue). (a) Tc 1, (b) LMC 56, (c) SMC 16, and (d) Lin 49. The spectra of Tc 1, LMC 56 and SMC 16, and Lin 49 are adapted from Cami et al. (2010), Bernard-Salas et al. (2012), and Otsuka et al. (2016). The excitation temperatures and mass derived from the thermal emission models based on a microcanonical ensemble are indicated at the left in each panel. The models have taken into account the uncertainties of DFT-predicted frequencies to align with the observation (see Details on the Astronomical Data section of the Appendix). Note that the $7.0\ \mu m$ bands in Tc 1 and SMC 16 contain a 15% contribution of the [Ar II] line (Bernard-Salas et al. 2012). Blue and gray dashed lines indicate the four observational C_{60} bands and strong atomic emission lines, such as [Ne II] ($12.81\ \mu m$) and [Ne III] ($15.55\ \mu m$) (Cami et al. 2010), respectively. The emission plateau between 11 and $13\ \mu m$ (strong in Tc 1, SMC 16, and Lin 49 but weaker in LMC 56)—indicated with a gray horizontal arrow—is generally attributed to and nominally labeled as SiC (Bernard-Salas et al. 2012), although the different profiles and substructures of the plateau suggest other carriers may also be present (García-Hernández et al. 2011). One possibility is that they may be due to the collective out-of-plane bending modes emitted by a mixture of aliphatic side groups attached to aromatic rings (Kwok et al. 2001). (e) Laboratory infrared spectrum of $C_{60}Fe^+$. (f) Summed theoretical spectrum of $[C_{60}\text{-Metal}]^+$. Here, blue dashed lines indicate the DFT-calculated frequencies of the four neutral C_{60} bands.

Here, we find that $[C_{60}\text{-Metal}]^+$ complexes could potentially (a) regulate the ratios of the four C_{60} bands by the variation of their spectral intensities for different metals (Figure A1), (b)

explain the shoulders and asymmetric band profiles observed in the $17\text{--}20\ \mu m$ region, and (c) explain several other yet unidentified features.

Table 2
Cross-correlation Coefficients

PNe	C ₆₀ Fe ⁺	C ₆₀ V ⁺	C ₆₀ H ⁺	C ₆₀ Fe ⁺	C ₆₀ V ⁺	C ₆₀ H ⁺	C ₆₀	C ₆₀ ⁺	C ₆₀ C ⁺
	Laboratory Band Position and DFT Intensity				DFT Band Position and Intensity				
Tc 1	0.65	0.75	0.47	0.67	0.76	0.53	0.82	0.38	0.55
LMC 56	0.74	0.82	0.60	0.75	0.83	0.65	0.85	0.50	0.70
SMC 16	0.67	0.72	0.68	0.72	0.70	0.70	0.66	0.64	0.67
Lin 49	0.68	0.70	0.78	0.74	0.69	0.80	0.56	0.74	0.82

Note. The calculated r values for C₆₀Fe⁺, C₆₀V⁺, C₆₀H⁺, C₆₀, C₆₀⁺, and C₆₀C⁺ templates and the observational Spitzer PNe data of Tc 1, LMC 56, SMC 16, and Lin 49.

In the 17–20 μm region, the laboratory spectra of both C₆₀Fe⁺ and C₆₀V⁺ show two intense bands at 17.4 and 18.8 μm with smaller features at 17.8 and 18.1 μm . Although it should be noted that for C₆₀V⁺ the laboratory feature at 18.8 μm partially overlaps with D₂-tag-induced bands at 19.3 and 19.8 μm (asterisks in Figure A1(b)), hindering the identification of pure C₆₀V⁺ features in the laboratory experiment, our calculations do show an asymmetric profile for the 19 μm band (Figure A1(c)). In addition, the laboratory spectral feature of C₆₀Fe⁺ at 18.8 μm is also asymmetric with a small shoulder around 19.5 μm .

In the 10–17 μm region of the laboratory spectra of both C₆₀Fe⁺ and C₆₀V⁺, there are several well-resolved features. Most of them coincide with features in LMC 56 including features superimposed on the 11–13 μm plateau and several with features in Tc 1, SMC 16, and Lin 49, within 0.1–0.2 μm intervals (Table 1). Exceptions are that no clear indications are seen in the observations for the 13.5 and 14.3 μm features of C₆₀Fe⁺. Note that in the laboratory spectrum, multiphoton absorption and saturation may strongly influence the amplitude of the observed transitions, which is why calculated single-photon intensity profiles are considered more trustworthy. The small wavelength differences could well be accounted for, considering that even for the C₆₀ bands in Tc 1 there is about a 1% deviation between laboratory and observational band positions (Cami et al. 2010). Besides known atomic lines (Table 1), to date, no confirmed carriers could explain the emission features in this spectral region, except for a possible contribution of C₆₀⁺ to the 10.5 μm band (Berné et al. 2013). The presence of C₇₀ and its contribution to emission features in those objects, except for Tc 1 (Cami et al. 2010), were proposed but are uncertain (García-Hernández et al. 2011; Bernard-Salas et al. 2012; Otsuka et al. 2016).

Apart from the two features at 7.0 and 8.5 μm coinciding with neutral C₆₀ bands, our laboratory spectra of both C₆₀Fe⁺ and C₆₀V⁺ also show other clear features in the 6–10 μm region that could have observational counterparts within 0.1 μm (Table 1). The exception is the laboratory double-peak feature of C₆₀V⁺ at 9.1 and 9.3 μm , which may be hidden in the broad emission plateau (particularly in SMC 16 and Lin 49; see Figure A4). Although C₆₀⁺ has been suggested to potentially contribute to UIE features at 6.4, 7.1, and 8.1 μm (Berné et al. 2013), it seems the observational emission bands, for example, the asymmetric profile of the intense 7.0 μm band of LMC 56, are better explained by [C₆₀-Metal]⁺ complexes. Brieva et al. previously tentatively assigned the feature at 6.49 μm to a combination mode of neutral C₆₀, but importantly they also proposed that it could be due to the formation of fullerene-metal complexes (Brieva et al. 2016), which now gains experimental support from our laboratory experiments.

To support this proposition, we quantify the similarity between each of the four PNe spectra and the laboratory C₆₀Fe⁺ spectrum by the cross-correlation coefficient, r , of the observational data with a C₆₀Fe⁺ template, and the template is constructed using laboratory-measured band positions and DFT-calculated intensities (see Details on the Astronomical Data section of the Appendix). Table 2 summarizes the calculated coefficients, which are also indicated in Figure A5. The same procedure is used to quantify the cross-correlation of the observational spectra and the laboratory spectra of C₆₀V⁺ and C₆₀H⁺ (Table 2 and Figures A4–A6). We additionally calculated the cross-correlation coefficients for similar template functions of C₆₀Fe⁺, C₆₀V⁺, C₆₀H⁺, C₆₀, and C₆₀⁺, utilizing only DFT-calculated quantities (positions and intensities; Table 2 and Figures A7–A10). Those analyses show that C₆₀ and C₆₀-metal complexes have r values close to 0.70–0.80, indicating a strong positive linear relationship, while C₆₀H⁺ and C₆₀⁺ only have a moderate linear relationship with the Spitzer PN spectra except for Lin 49 (Otsuka et al. 2016). Moreover, since C₆₀ may accrete by absorbing a carbon atom to form C₆₀C⁺ (Omont 2016), similar to [C₆₀-Metal]⁺ complexes, we also did the same type of analysis for C₆₀C⁺, and the results in Table 2 and Figures A7–A10 show that the r values for C₆₀C⁺ are not better than [C₆₀-Metal]⁺ complexes except for Lin 49. This provides statistical support for the appearance of [C₆₀-Metal]⁺ complexes in the Spitzer data, at a level similar to or slightly higher than the statistical confidence of C₆₀, C₆₀⁺, C₆₀H⁺ in Tc 1, LMC 56, and SMC 16 (Palotás et al. 2020). It is consistent with our estimates based on collision theory that [C₆₀-Metal]⁺ complexes could form and survive in space.

Closer inspection of Figure 2 and Figures A4 and A5 allows us to pinpoint the wavelength regions between 6–9 and 13–15 μm and the asymmetric profiles in the 17–20 μm region as potentially diagnostic for the presence of [C₆₀-Metal]⁺. The characteristic features are identified to be due to the presence of metal on the C₆₀ cage, which perturbs the vibronic energy levels of C₆₀ both geometrically and electronically (Figures A11–A13). Our laboratory spectra also show features at 22.9–23.4 μm for C₆₀Fe⁺ and at 23.5 μm for C₆₀V⁺, attributed to metal–C₆₀ cage stretching vibrations, which may have weak coinciding bands in LMC 56, SMC 16, and Lin 49. Similarly, the laboratory double-peak feature of C₆₀Fe⁺ at 20.2 and 20.6 μm might be reflected particularly in SMC 16 and Lin 49 (highlighted in light yellow in Figure A5). However, the current quality of the observation and the experiment in this wavelength range precludes a firm identification. The exact spectral positions of such metal–cage stretching vibrations depend on the specific metals as shown by our DFT

calculations (Figures A3 and A14) and could serve as potential signatures to characterize and quantify a specific $[C_{60}\text{-Metal}]^+$ complex. The metal- C_{60} vibrational modes beyond $30\ \mu\text{m}$ are even more metal-specific (Figures A3 and A12).

4. Discussion

The experimental work in this contribution is limited to the mid- to far-infrared spectral range. At shorter wavelengths, ranging from near-infrared to ultraviolet, $[C_{60}\text{-Metal}]^+$ also offers a wealth of electronic transition lines that could be potential candidates for DIBs. Because no experimental work exists for $[C_{60}\text{-Metal}]^+$ in these spectral ranges, we only note that, in comparison to C_{60}^+ , recently identified as a carrier of several DIBs (Campbell et al. 2015; Maier & Campbell 2017; Cordiner et al. 2019), for $[C_{60}\text{-Metal}]^+$ many more electronic transition lines are predicted in our time-dependent DFT (TDDFT) calculations (Figure A13). It should be pointed out that TDDFT is currently not capable of accurately predicting the exact energies of the electronic absorption bands, and the lack of experimental benchmark data hampers a quantitative comparison between theory and the DIB observations.

The origin and formation mechanisms of fullerenes in space are still mysterious (Woods 2020; Kwok 2022). Recalling the catalytic roles of metals in the nucleation and growth of various carbon nanostructures, including carbon nanotubes (Esconjauregui et al. 2009) and carbon cages under oxygen- and hydrogen-rich conditions (Dunk et al. 2013, 2014), we conjecture that the presence of fullerene-metal complexes can link the chemical pathways and mechanisms of the formation and evolution of various carbonaceous species and thus carbon chemistry in space. Furthermore, one may even conjecture that a fraction of identified C_{60} fullerene lines actually may stem from fullerene-metal complexes. To substantiate this argument, we have determined the temperature and abundance required for each species to replicate the observed emission spectra of the four fullerene-rich PNe using thermal emission models that treat the fullerene-metal complexes as a microcanonical ensemble (Figure 2). About $2.6\text{--}7.7 \times 10^{-8}$ solar mass (M_\odot) of pure C_{60} is required to reproduce the four main emission bands. An equally good fit, which also accounts for some additional emission features, is obtained for $\sim 0.69\text{--}2.1 \times 10^{-7} M_\odot$ of $C_{60}\text{Fe}^+$, or $\sim 1.9\%\text{--}6.1\%$ of the available carbon with excitation temperatures above ~ 400 K. Arguably, these diffuse nebulae do not disfavor the ionized form of gaseous C_{60} and $C_{60}\text{Fe}$ owing to their low ionization potentials, but it is challenging to accurately estimate the fractions considering the complicated charge balance, i.e., competition among ionization, electron attachment, and recombination events as well as the lack of parameters associated with those processes (see Photodissociation Rates section of the Appendix). This argument together with the high cross-correlation coefficients and good fits of the thermal emission model supports the inference that gaseous ionized fullerene-metal complexes are potentially good candidates for explaining the infrared emission spectra of these four PNe in addition to neutral C_{60} . The forthcoming high-resolution and high-sensitivity data from the James Webb Space Telescope can provide better constraints on the environmental conditions of specific fullerene-metal complexes and their abundances, of crucial importance for revealing the dominant chemical pathways, and in particular the initial steps of fullerene formation in the universe.

Acknowledgments

This work is supported by the KU Leuven Research Council (C1 grants C14/22/103 and MAESTRO C16/17/007), the Research Foundation Flanders (AKUL/15/16 G0H1416N and G0A0519N), the project CALIPSOplus under grant agreement 730872 from the EU Framework Programme for Research and Innovation HORIZON 2020. L.D. acknowledges support from the ERC-CoG grant 646758, and G.L.H. acknowledges support from the National Natural Science Foundation of China (92261101), the Innovation Capability Support Program of Shaanxi Province (2023-CX-TD-49), and Xi'an Jiaotong University. The computational resources and services used in this work were provided by the VSC (Flemish Supercomputer Center), funded by the Research Foundation–Flanders (FWO) and the Flemish Government–department EWI. We gratefully acknowledge the Nederlandse Organisatie voor Wetenschappelijk Onderzoek (NWO) for the support of the FELIX Laboratory and thank the FELIX staff. G.L.H. thanks Profs. Yong Zhang (Sun Yat-sen University) and Hong Gao (Chinese Academy of Sciences) for helpful discussions, and Dr. Alessandra Candian (University of Amsterdam) for providing the Spitzer data files in Figure 2. We also thank Prof. Alexander Tielens (Leiden University) for useful suggestions and Drs. Jan Vanbuel and Piero Ferrari for assistance in adapting the laser vaporization source with the molecular beam setup at FELICE.

Author Contributions

G.L.H. conceived and coordinated the work, performed the IRMPD experiments with O.V.L. and J.M.B., formulated the idea of this work from discussions with E.J., P.L., and L.D., and conducted the theoretical calculations and modeling. G.L.H. calculated the formation and dissociation rates, L.D. did the cross-correlation and abundance analyses, and J.M.B. did the normal mode decomposition analysis. G.L.H. wrote the manuscript with comments and inputs from E.J., L.D., J.M.B., and P.L. E.J., G.L.H., and P.L. obtained the funding for this research.

Competing interests: The authors declare no competing interests. An earlier version of this work is available at arXiv:[2207.10311](https://arxiv.org/abs/2207.10311).

Appendix Details of Methods

Experimental. The $[C_{60}\text{-Metal}]^+$ (Metal = Fe and V) complexes are synthesized in vacuum by a dual-target dual-laser ablation source, which is a modified version of the Smalley-type laser vaporization source used in the discovery of C_{60} in 1985 (Kroto et al. 1985) and has been described in detail previously (Ferrari et al. 2017). The choice of iron and vanadium as representative examples in the experiment is motivated by the fact that (i) both iron and vanadium have been detected in many astrophysical environments (Baluteau et al. 1995; Kaminski et al. 2015; Omont 2016), and (ii) the synthesis of $C_{60}\text{Fe}^+$ and $C_{60}\text{V}^+$ is stable, facilitating the infrared experiment. Both the bulk metal and the C_{60} -fullerene targets are vaporized by 532 nm laser pulses from two independent Nd:YAG lasers, both operated at 10 Hz repetition rates. The vaporized neutral C_{60} molecules and metal plasma, containing metal cations, collide with each other in the presence of He gas, introduced through a pulsed valve with a 6 bar stagnation

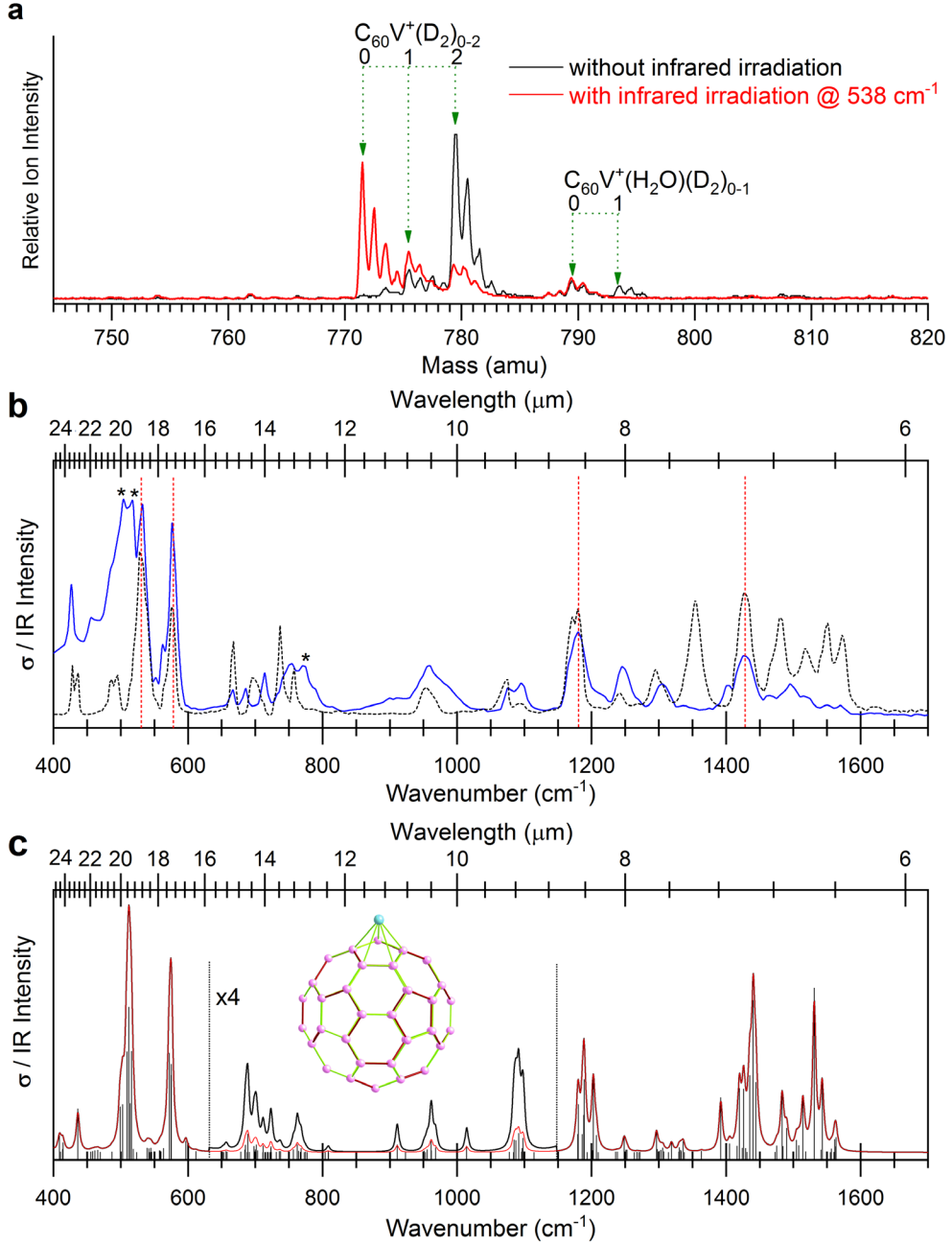


Figure A1. Laboratory synthesis and infrared spectroscopy of C_{60}V^+ . (a) Mass distributions of C_{60}V^+ and its D_2 -tagged complexes synthesized using a dual-target dual-laser vaporization source, with (red) and without (black) the infrared irradiation at 538 cm^{-1} . (b) IRMPD spectrum of D_2 -tagged C_{60}V^+ (solid blue curve) and its comparison with that of Ar-tagged C_{60}Fe^+ (dotted black curve) in the 400–1700 cm^{-1} range. The positions of four neutral C_{60} bands are indicated with vertical red dotted lines; the asterisks mark the features mainly induced by D_2 (Figures A15–A16). (c) Theoretically simulated spectrum of C_{60}V^+ at the BPW91/6-31G(d) level (red curve) with its calculated structure shown as an inset. The calculated intensities are plotted with sticks and convolved using Lorentzian line shapes of 6 cm^{-1} FWHM. The convolved spectrum is also enlarged by a factor of 4 between 650–1150 cm^{-1} (black curve). The comparison shows that the spectral patterns of C_{60}Fe^+ and C_{60}V^+ have similar characteristic features except that the spectrum of C_{60}V^+ shows several D_2 -involved modes and their intensities vary, likely due to multiple photon excitation effects (see detailed band positions in Table 1).

pressure, which triggers the formation and cooling of the complexes. We assume $[\text{C}_{60}\text{-Metal}]^+$ complexes to be thermalized to room temperature before expansion into vacuum, moderately cooling their internal degrees of freedom.

The high stabilities of C_{60}Fe^+ and C_{60}V^+ , characterized by the 2.25 and 2.82 eV binding energies between C_{60} and Fe^+ and V^+ , respectively, (corresponding to approximately 20 photons at 10 μm) prevent the recording of high-quality IR spectra over the full wavelength range. Only a few IR features of large calculated IR oscillator strengths show up with a low

signal-to-noise ratio (S/N) (see, for example, the C_{60}V^+ case in Figure A17). Therefore, the messenger tagging technique was utilized, with Ar as the tag for C_{60}Fe^+ and D_2 for C_{60}V^+ . This technique has been well established in past decades to obtain the vibrational or electronic spectra of molecular species via photodissociation (Campbell et al. 2015; Roithová et al. 2016; Yang et al. 2019; Hou et al. 2021; Li et al. 2022). Ar-tagged C_{60}Fe^+ (calculated binding energy is negligible) was formed by seeding about 5% Ar into the He carrier gas; for D_2 -tagged C_{60}V^+ (0.3–0.4 eV, or 3 photons at 10 μm), a 0.5% D_2 seeding

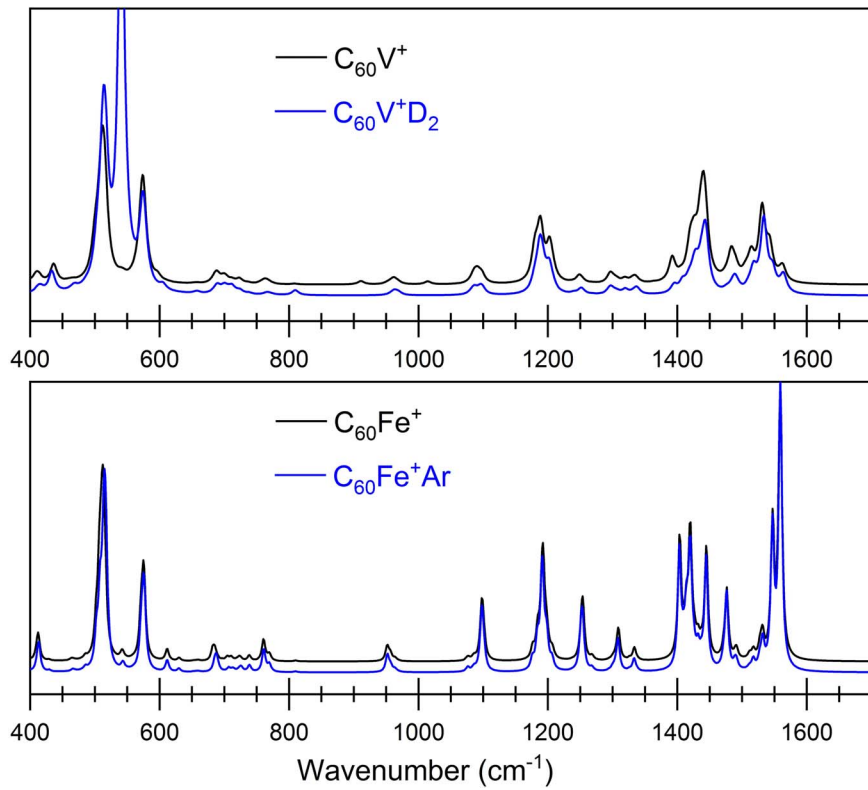


Figure A2. Overlaid simulated spectra of $C_{60}V^+$ with and without the D_2 tag and of $C_{60}Fe^+$ with and without the Ar tag. A comparison of the DFT calculations on the C_{60} -metal complexes with and without tags (D_2 or Ar) supports the conjecture that tagging has a small effect on the vibrational frequencies. In the case of $C_{60}V^+$, using D_2 as a tag, the appearance of new features around 540 and 810 cm^{-1} is due to D_2 (see Figure A1).

was used. After expansion into vacuum through a conical nozzle, the cluster beam is formed and shaped by a 2 mm diameter skimmer and a 2 mm slit aperture, before entering into the extraction zone of a perpendicular reflectron time-of-flight (TOF) mass spectrometer.

IRMPD experiments are performed by overlapping the shaped cluster beam with the IR light of FELICE (Bakker et al. 2010). The measurements were conducted with two FEL settings, covering the 400 – 850 and 700 – 1700 cm^{-1} spectral ranges, at a repetition rate of 5 Hz. This allowed us to record successive mass spectra with and without IR laser interaction. Laser excitation in resonance with a vibrational mode heats up the clusters by multiple photon absorption and intramolecular vibrational redistribution (IVR). When the internal energy of the cluster is high enough, fragmentation (dissociation) takes place on the timescale of the experiment via the lowest-energy fragmentation channel, in the current case, desorption of Ar from $C_{60}Fe^+\bullet\text{Ar}$ or of D_2 from $C_{60}V^+\bullet(D_2)_{1,2}$. Here, the Ar atom and D_2 molecule serve as non-interfering weakly bound messengers that will be shed if IR radiation is resonantly absorbed, representing a sensitive probe by mass spectrometry. Care has been taken with the FEL light focusing to minimize saturation effects and to avoid destruction of the C_{60} cage, which is confirmed by the absence of C_{60-2m}^+ fragments.

Nevertheless, the IRMPD spectroscopy requiring the absorption of more than one photon may hamper the interpretation of observed intensities as a direct reflection of the linear absorption cross sections. IRMPD spectra approach linear absorption spectra if the dissociation energy is lower than the energy carried by the photon absorbed. Here, the binding energy of D_2 is higher than the photon energy, making the one-

to-one comparison between the experimentally observed intensities uncertain. Also, linear absorption spectra have a large dynamic range: When observing weaker IR bands, it is possible that the strongest bands are already saturated, something that is likely the case for the bands at 17.4 and $18.9\text{ }\mu\text{m}$. The experimental frequencies of the absorptions are less prone to strong deviations from linear absorption than the experimental intensities.

Quantum chemical calculations, on the other hand (see the Theoretical section below), provide linear absorption spectra, calculated in the approximative harmonic approach. The potential energy surface from which the IR intensities are derived depends on the choice of exchange-correlation functional. Consequently, extracting the “true” absorption cross sections requires a type of self-consistent field approach, where each time the shortcomings of one should be balanced against the other. One of the ingredients in this process is the evaluation of the results of different exchange-correlation functionals (see Figure A18). Consequently, as the best possible approach, we have opted to combine experimental frequencies with calculated intensities, which we consider the most reasonable compromise between theory and experiment.

The FEL was scanned in wavenumber steps of 5 cm^{-1} , which implies a nonconstant step size in wavelengths of 0.03 – $0.05\text{ }\mu\text{m}$ below $10\text{ }\mu\text{m}$ (above 1000 cm^{-1}), $0.1\text{ }\mu\text{m}$ around 800 cm^{-1} ($12.5\text{ }\mu\text{m}$), and $0.2\text{ }\mu\text{m}$ around 500 cm^{-1} ($20\text{ }\mu\text{m}$). The IR wavelength is calibrated using a grating spectrometer, with a typical uncertainty of the FEL wavelength of 0.2% .

The experiments allow us to obtain IR spectra by comparing the mass spectrometric intensities of $[C_{60}\text{-Metal}]^+$ and its messenger-tagged complexes with $[I(\nu)]$ and without (I_0) FEL

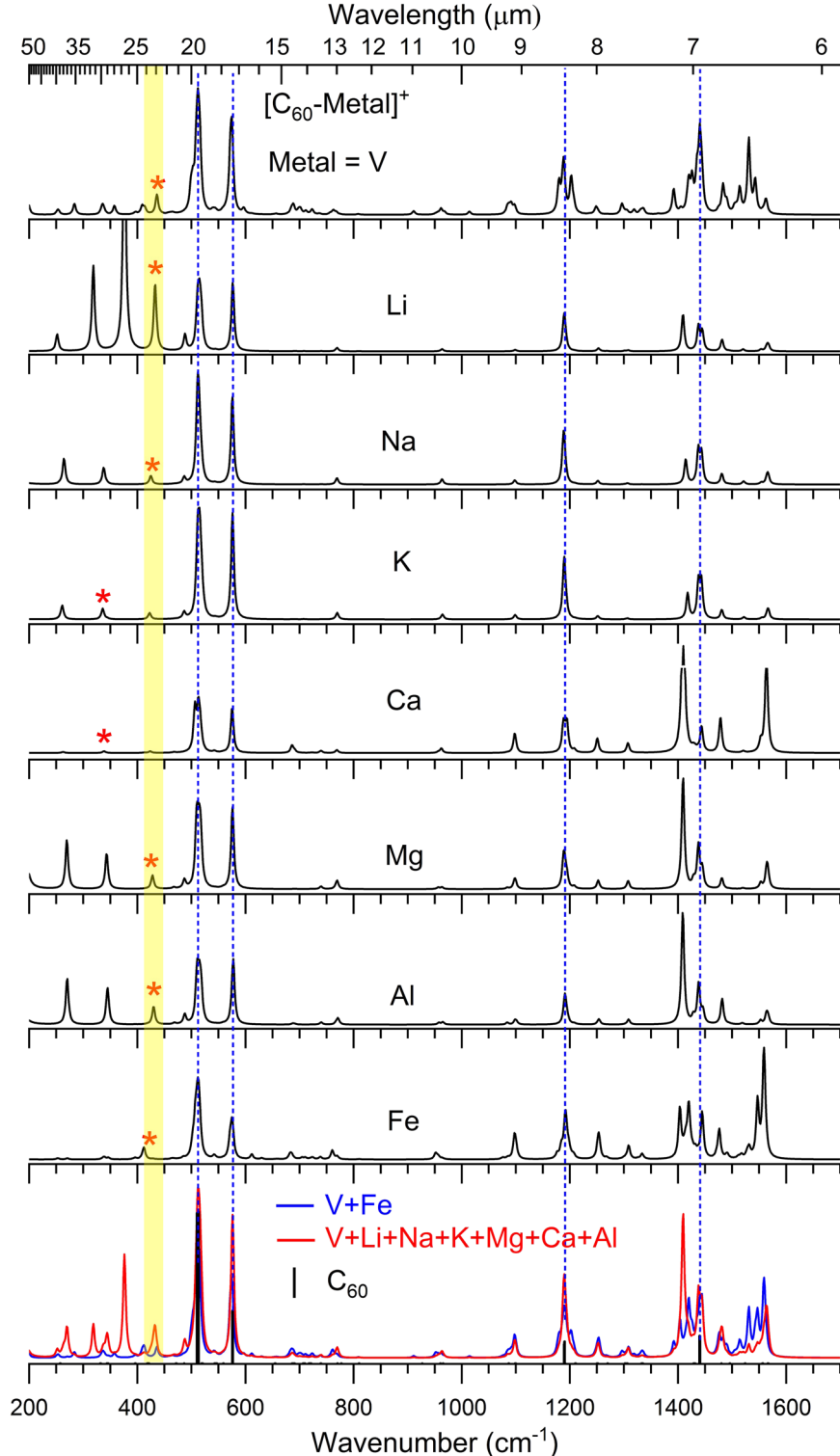


Figure A3. Simulated infrared spectra of the most stable $[C_{60}\text{-Metal}]^+$ (Metal = V, Li, Na, K, Mg, Ca, Al, and Fe) and the stick spectrum showing the four neutral C_{60} bands at the BPW91/6-31G(d) level of theory. The blue dashed lines show the coinciding features of $[C_{60}\text{-Metal}]^+$ with the four C_{60} bands but with different intensity ratios. The spectra are convolved using Lorentzian line shapes of 6 cm^{-1} FWHM. They all show similar infrared spectral patterns regarding both the band positions and relative intensities. The small differences are due to different metals perturbing C_{60} at different extents both geometrically and electronically. The average spectra for all metals and for vanadium and iron are also provided, and it can be seen that the averaged spectra of $[C_{60}\text{-Metal}]^+$ are similar to that of $C_{60}\text{V}^+$, except that the intensities of a few features, for example, those at $680, 1100, 1420, 1540\text{ cm}^{-1}$, vary and slightly shift within a few wavenumbers. Such comparison supports the idea of utilizing the experimental infrared spectrum of $C_{60}\text{V}^+$ as a representative model of various $[C_{60}\text{-Metal}]^+$ complexes to discuss their infrared spectral features. The asterisks (also highlighted with the yellow bar) indicate the vibrational modes due to metal- C_{60} cage stretching, and their vectors are presented in Figure A14. Note that the $C_{60}\text{K}^+$ and $C_{60}\text{Ca}^+$ complexes have the metal- C_{60} stretching modes at lower frequencies ($\sim 340\text{ cm}^{-1}$).

light irradiation. The IRMPD yield is defined as the depletion ratio of $I(\nu)/I_0$,

$$Y(\nu) = I(\nu)/I_0. \quad (1)$$

To reduce the noise originating from cluster synthesis fluctuations, we first calculate the branching ratio B of the number of $C_{60}Fe^+Ar_1$ ions to all $C_{60}Fe^+Ar_{0,1}$ ions, or $C_{60}V^+(D_2)_2$ ions to all $C_{60}V^+(D_2)_{0-2}$ ions:

$$B = I[C_{60}Fe^+Ar]/\sum I[C_{60}Fe^+Ar_{0,1}], \quad (2)$$

$$B = I[C_{60}V^+(D_2)_2]/\sum I[C_{60}V^+(D_2)_{0,1,2}]. \quad (3)$$

Under the assumption of constant Ar or D_2 adsorption rates, this eliminates fluctuations in the synthesis. We then calculate the depletion yield Y' as a function of IR frequency ν by taking the natural logarithmic ratio of the branching ratios with and without IR irradiation,

$$Y'(\nu) = -\ln[B(\nu)/B_0]. \quad (4)$$

The depletion yield $Y'(\nu)$ is divided by the laser pulse energy $E(\nu)$ to account for the variation of the laser power (but note that this will not correct the intensity issues intrinsic to the multiphoton process) and to approximate the infrared absorption cross section,

$$\sigma(\nu) = Y'(\nu)/E(\nu). \quad (5)$$

The FEL laser pulse energy is reconstructed by measuring the pulse energy of a fraction of the pulse that is outcoupled from the FELICE cavity (Bakker et al. 2010). Typical pulse energies used range from 1000 mJ at 400 cm^{-1} to 200 mJ at 1600 cm^{-1} .

To confirm there are no other dissociation channels in the $C_{60}V^+$ experiment apart from D_2 desorption, the laser-induced changes of the ion intensity and the summed ion intensity of $C_{60}V^+(D_2)_{0-2}$ with and without IR light irradiation are plotted in Figure A19 as a function of IR wavelength. It is obvious that the vast majority of the gained $C_{60}V^+$ signal arises from $C_{60}V^+(D_2)_2$ depletion, while the summed ion intensity is conserved within the experimental uncertainty. A similar procedure has been conducted for the experiments with $C_{60}Fe^+$.

Without D_2 tagging, only a few features of high calculated oscillator strengths are observed in the infrared spectrum of $C_{60}V^+$ in the 1100–1600 cm^{-1} range (Figure A17). These indicate that the perturbation of the D_2 tag on the vibrational band positions of $C_{60}V^+$ is negligible, which is confirmed by DFT calculations on the infrared spectra of $C_{60}V^+$ and its D_2 -tagged complexes in the 400–1700 cm^{-1} range (Figure A15). The calculations show that the main changes induced by the D_2 tag are that strong vibrational features around 510, 540, and 830 cm^{-1} , which significantly involve D_2 motions, show up (Figure A16). For the experiments on $C_{60}Fe^+$, not much influence of Ar has been found in the studied spectral range. Hence, the IRMPD spectra of messenger-tagged $C_{60}V^+$ and $C_{60}Fe^+$ can be regarded as the IR absorption spectra of $C_{60}V^+$ and $C_{60}Fe^+$.

Theoretical. For $C_{60}V^+$, five structures, i.e., η^5 , η^6 , $\eta^{2(6-6)}$, $\eta^{2(6-5)}$, and η^1 , have been fully optimized to obtain its most stable structure. In those structures, the V atom binds with the hexagonal center, pentagonal center, bridge of a hexagon and a hexagon, bridge of a hexagon and a pentagon, and atop of C_{60} , respectively. Since the electron configuration of the V atom is $[\text{Ar}]3d^34s^2$ and the ground state of V^+ is $[\text{Ar}]3d^34s^1$, the interaction of V^+ with the closed-shell molecule C_{60} to form

$C_{60}V^+$ could result in $S = 0, 1, 2$ spin states. Hence, for each structure, these spin states were considered. During the structure optimization, the η^1 structure was unstable and converged to either η^5 or η^6 in all three spin states. Three functionals, i.e., BPW91, PBE, and B3LYP, were employed to test the reliability of DFT calculations. All three functionals calculate the η^5 structure in the $S = 2$ spin state to be the most stable one (Table A3). Similar calculations have been performed for $C_{60}Fe^+$, for which the η^5 structure with $S = 5/2$ was the most stable. From the comparison in Figure A18, it can be seen that overall, BPW91 provides the best agreement between the calculated IR spectrum and experiment, consistent with previous findings on the good performance of this functional in calculating vanadium-carbon binary clusters (Yuan et al. 2016; Hou et al. 2021; Li et al. 2022). Due to the large size of the studied complex, double- ζ quality basis sets (6-31G(d) and/or def2-SVP) were used for all calculations. Triple- ζ quality basis sets (6-31G(d), def2-TZVP, and Lanl2TZ) were also checked, showing consistent results with the double- ζ basis sets (Figure A20). Therefore, the BPW91/6-31G(d) method was employed to do the calculations for C_{60} , C_{60}^+ , and $[C_{60}\text{-Metal}]^+$ (Metal = H, Li, Na, K, Mg, Ca, Al, and Fe) as well as for $C_{60}C^+$. The harmonic approximation was employed to perform the vibrational analysis of the calculated structures. The vibrational analysis is used on one hand to confirm that the calculated structures are real minima and on the other hand to simulate theoretical IR spectra to compare with the measured IRMPD spectra. All calculations were conducted with the Gaussian 09 program package (Frisch et al. 2013).

Details on the Astronomical Data and the Cross-Correlation Analysis. The Spitzer infrared spectra of Tc 1, LMC 56 and SMC 16, and Lin 49 are adapted from Cami et al. (2010), Bernard-Salas et al. (2012), and Otsuka et al. (2016). They were all recorded by the Infrared Spectrograph (IRS) on board the Spitzer Space Telescope. For Tc 1, the entire spectrum consists of observations at low-resolution mode ($\lambda/\Delta\lambda \sim 60$ –120) with the Short-Low module (SL, 5.2–14 μm ; $\Delta\lambda \sim 0.04$ –0.12 μm), and at high-resolution mode ($\lambda/\Delta\lambda \sim 600$) with the Short-High (SH, 9.8–19.5 μm ; $\Delta\lambda \sim 0.02$ –0.04 μm) and Long-High (LH, 19.5–36 μm ; $\Delta\lambda \sim 0.04$ –0.06 μm) modules. For LMC 56, SMC 16, and Lin 49, all spectra were recorded at low resolution using the SL and Long-Low (LL) modules. In the current work, all Spitzer data have been rebinned to the wavelength grid of SMC 16 using linear interpolation for ease of comparison. Note this rebinning process may smear out a few sharp atomic lines, in particular for the high-resolution spectral region (9.8–19.5 μm) of the Spitzer data of Tc 1 (Cami et al. 2010), but it will not affect the following analysis. For more details about those observational data, please refer to Cami et al. (2010), Bernard-Salas et al. (2012), and Otsuka et al. (2016).

The Spitzer data of the four PNe (Tc 1, LMC 56, SMC 16, and Lin 49) have a high S/N with a typical rms value of $\sim 1\%$ below $\sim 14 \mu\text{m}$ and $\sim 5\%$ –20% for ~ 14 –25 μm . However, the spectral resolution of the Spitzer data is not high enough, except for Tc 1 in the 9.8–36 μm spectral range, to spectrally resolve individual molecular emission lines. Hence, the largest uncertainty for the detection of spectral fingerprints is steered by uncertainties in the continuum subtraction (Cami et al. 2010) and the fact that other molecules and dust species contribute to the overall spectrum as well. That uncertainty,

σ_{cont} , is quantified by the standard deviation of the flux in the wavelength region between 20.1 and 21.7 μm . For a molecule with a number of N spectral fingerprints in a particular wavelength region, the 3σ detection limit can be estimated as $3\sigma_{\text{cont}}/\sqrt{N}$. In Figures A4–A10, the thickness of the horizontal, light gray lines indicates the 3σ detection limit for the fingerprints of the metal complexes.

The similarity between each of the four Spitzer PN spectra and laboratory infrared spectra is quantified by the cross-correlation coefficient, which is a preferred and well-established method of choice for the analysis of one component in a complex system (Koenig 1999). For instance, it has been used for detecting chemical species in exoplanet atmospheres (Hoeijmakers et al. 2018, 2019) or for the study of C_{60}^+ diffuse interstellar band correlations and environment variations (Schlarmann et al. 2021). Here, it is $[\text{C}_{60}\text{-Metal}]^+$ in the PNe with varying chemical compositions and thermodynamic properties. The cross-correlation coefficient of two sample populations, X and Y , as a function of the lag (L) is calculated as

$$r(L) = \begin{cases} \frac{\sum_{k=0}^{N-|L|-1}(x_{k+|L|} - \bar{x})(y_k - \bar{y})}{\sqrt{\left[\sum_{k=0}^{N-1}(x_k - \bar{x})^2\right]\left[\sum_{k=0}^{N-1}(y_k - \bar{y})^2\right]}} & \text{for } L < 0 \\ \frac{\sum_{k=0}^{N-L-1}(x_k - \bar{x})(y_{k+L} - \bar{y})}{\sqrt{\left[\sum_{k=0}^{N-1}(x_k - \bar{x})^2\right]\left[\sum_{k=0}^{N-1}(y_k - \bar{y})^2\right]}} & \text{for } L \geq 0 \end{cases}, \quad (6)$$

where \bar{x} and \bar{y} are the means of the sample populations $x = (x_0, x_1, \dots, x_{N-1})$ and $y = (y_0, y_1, \dots, y_{N-1})$.

However, a direct calculation of the cross-correlation coefficient between observational Spitzer spectra and the laboratory spectra is not meaningful owing to (i) the multiphoton nature of the laboratory experiment that results in the experimental intensities not being a good measure of the line strength, and in the case of C_{60}V^+ , (ii) a few features significantly involve D_2 motions. These shortcomings can be overcome by using the outcome of DFT calculations, in particular the calculated line strengths. We recalibrated the laboratory spectra by taking the experimental band positions (but excluding the bands strongly involving D_2 motions for C_{60}V^+) and scaling the intensities to DFT calculations. In this step, we account for the laboratory spectral resolution determined by the scan step, σ_{lab} , or, if DFT-calculated frequencies are used, the $\sim 2\%$ uncertainty in DFT-calculated band positions (Laury et al. 2012). The outcome is then convolved with a Gaussian function with the FWHM being determined from the Spitzer spectral resolution, σ_{obs} . Finally, we assign the combined laboratory (or DFT) and Spitzer wavelength uncertainty, $\sqrt{\sigma_{\text{lab}}^2 + \sigma_{\text{obs}}^2}$, as the wavelength resolution to the new C_{60}Fe^+ or C_{60}V^+ template (red curves in Figures A4–A10) and calculate the cross-correlation coefficient of this template with the PN spectra; see Table 2. Note that since we allow the frequencies to move around given the uncertainty in lab/DFT frequencies and observational wavelength grid, the templates shown in Figures A4–A10 are slightly different from one source to the other. Entire spectra were employed for the cross-correlation analysis.

Abundance estimates. The Spitzer spectra of the four PNe allow for the abundance of the contribution species to be calculated. Since both C_{60} and C_{60}Fe^+ share the same most intense bands at 7.0, 8.5, 17.4, and 18.9 μm , a reliable relative abundance estimate of one species with respect to the other is

not possible. However, one can estimate the abundance of one species so that the predicted band intensities reproduce the observed spectra. We therefore follow the same methodology as Cami et al. (2010) by assuming a microcanonical thermal emission model. Instead of relying on experimentally obtained relative absorption coefficients for the C_{60} bands, we here exploit the DFT-calculated band intensities. For a thermal population distribution over the excited states, we determine the excitation temperature and total mass of each species following a χ^2 minimization procedure for the four main bands at 7.0, 8.5, 17.4, and 18.9 μm (Figure 2). We here account for the described deviation, which allows a shift around the calculated frequencies of maximally $\sim 2\%$ (Laury et al. 2012). For C_{60} , the excitation temperature ranges between ~ 470 –620 K, while the excitation temperature of C_{60}Fe^+ is lower for all targets and ranges between ~ 400 and 500 K. About $2.6 - 7.7 \times 10^{-8} M_\odot$ of pure C_{60} and $0.69 - 2.1 \times 10^{-7} M_\odot$ of C_{60}Fe^+ are required to reproduce the observed emission bands. At the measured carbon abundance for PNe in the galaxy, LMC, and SMC (Milanova & Kholtynin 2009), and assuming a mass-loss rate of $10^{-4} M_\odot \text{ yr}^{-1}$ over the past 100 yr (Cami et al. 2010), this implies that C_{60} represents $\sim 0.7\%$ – 2.3% of the available carbon, consistent with previous estimates for evolved stars in Table A1. Under the assumption that the emission bands are purely due to C_{60}Fe^+ , $\sim 1.9\%$ – 6.1% of the available carbon would be consumed by C_{60}Fe^+ .

Cami et al. derived a thermal excitation temperature of C_{60} in Tc 1 of 330 K (Cami et al. 2010), slightly lower than our value of 470 K. That low temperature allowed Cami et al. to argue that the emission does not originate from free molecules in the gas phase but from C_{60} formed on the surface of cool, solid material with the most likely composition being carbonaceous grains. In that case, the charge effects on individual molecules are negligible. For a typical effective temperature of $\sim 20,000$ K, the radiation field peaks for photon energies in the range of 6–10 eV. Hence, in contrast to solid fullerenes, gaseous C_{60} may be largely ionized owing to its low ionization potential of 7.61 eV (Foing & Ehrenfreund 1994). If these large gaseous clusters are free-flying species, temperatures above ~ 450 K can be readily reached via stochastic heating by absorption of a single UV photon (Zhang et al. 2017). The excitation temperature of C_{60} is highly uncertain owing to uncertainties in the Einstein A coefficients (Zhang & Kwok 2013), but most reported C_{60} sources have excitation temperatures well above 400 K, even reaching values of 1000 K, which may question the existence of C_{60} in solid form. Our simplified thermal modeling approach supports these higher excitation temperatures and hence supports the argument for the presence of gaseous fullerene-rich species. Taking the argument one step further, if C_{60} is in a gaseous form, a significant fraction could be ionized. Hence, neutral C_{60} , possessing only four active infrared features, alone cannot explain the infrared emission features here under study. However, it is challenging to accurately estimate the fractions considering the complicated charge balance, i.e., competition among ionization, electron attachment, and recombination events as well as the lack of parameters associated with those processes. The high correlation coefficients (Table 2), the good fits of the thermal emission model (Figure 2), and the low ionization potential of C_{60}Fe (ca. 6.34 eV) render the conjecture that gaseous ionized fullerene-metal complexes, in which C_{60} behaves as almost neutral, are equally good candidates as C_{60} for explaining the

Table A1
The Abundances of Fullerenes (Percent of Gas-phase Carbon Locked in Fullerene Species), Derived from Emission or Absorption Measurements in Star-forming Regions, Diffuse ISM, and Evolved Stars

Star-forming Regions		Diffuse ISM		Evolved Stars	
Emission	Absorption	Emission	Absorption	Emission	Absorption
C_{60}^+	0.01 ^a	...	0.2 ^c (upper limit)	0.06–0.1 ^e	...
C_{60}	0.04–0.06 ^b	...	0.03–0.4 ^e	...	0.1–3.0 ^d

Notes.

^a From Berné et al. (2013)

^b From Castellanos et al. (2014)

^c From Berné et al. (2017)

^d From Cami et al. (2011)

^e From Iglesias-Groth & Esposito (2013)

infrared spectra of the four PNe. However, more accurate Einstein A coefficients are required to draw solid conclusions.

Formation Rates of the $[C_{60}\text{-Metal}]^+$ Complexes. We employed collision theory to estimate the formation rates of $[C_{60}\text{-Metal}]^+$ complexes in space. Collision theory predicts the rate $r(T)$ of a bimolecular gas-phase reaction between reactants A and B at temperature T to be

$$r(T) = kn_A n_B = Z\rho \exp\left(\frac{-E_a}{RT}\right), \quad (7)$$

where k is the collisional rate constant in units of $\text{cm}^3 \text{ s}^{-1}$, n_A and n_B the number densities of A and B (in cm^{-3}), Z the collision rate (in $\text{cm}^{-3} \text{ s}^{-1}$), ρ the steric factor, which reflects the reaction probability depending on the mutual orientations of the reactant particles, E_a the activation energy of the reaction, and R the ideal gas constant.

For two neutral particles, the collision rate can be approximated by a hard-sphere model,

$$Z = n_A n_B \sigma_{AB} \sqrt{\frac{8k_B T}{\pi \mu_{AB}}}, \quad (8)$$

where $\sigma_{AB} = \pi(r_A + r_B)^2$ is the collision cross section with r_A and r_B the radii of A and B, k_B the Boltzmann constant, and μ_{AB} the reduced mass of A and B. Assuming that there is no activation energy, i.e., $E_a = 0$, for the AB complex formation, and that the steric factor ρ equals 1, the hard-sphere collisional rate constant can be simplified as

$$k_{HS} = \sigma_{AB} \sqrt{\frac{8k_B T}{\pi \mu_{AB}}} = 4.65 \times 10^{-12} (r_A + r_B)^2 \sqrt{\frac{T}{\mu_{AB}}}, \quad (9)$$

with r_A and r_B in angstroms, T in K, μ_{AB} in atomic mass units, and k_{HS} in $\text{cm}^3 \text{ s}^{-1}$.

For a collision between an ion and a small neutral particle without activation energy ($E_a = 0$), the rate constant k_L is described by the Langevin model,

$$k_L = 2\pi e \sqrt{\frac{\alpha}{\mu_{AB}}} = 2.34 \times 10^{-9} \sqrt{\frac{\alpha}{\mu_{AB}}}, \quad (10)$$

where e is the elementary charge in cgs units (statcoulombs), α the polarizability of the neutral particle in cgs units (\AA^3), and k_L in units of $\text{cm}^3 \text{ s}^{-1}$. The polarizability of C_{60} , $\alpha \approx 80 \text{\AA}^3$, and the radius of C_{60} is 5.09 \AA . The radii of the ionized metals are slightly smaller than their atomic radii.

Here, it should be noted that assuming no activation energy and facile conversion of the binding energy to thermal energy, distributed over the 177 vibrational modes of the fullerene-metal complex, the unimolecular dissociation rate (see below) will be extremely low and the Langevin collision rate is a good proxy for the formation rate.

Table A4 lists the metal abundances that we investigated in this work, and Table A1 summarizes the abundances of fullerenes by percent of gas-phase carbon locked in fullerene species in different astrophysical environments. Depending on the sources, the metal abundances are in the range of $\sim(5 \times 10^{-11}–3.2 \times 10^{-5}) \cdot n_H$, with n_H the number density of atomic hydrogen. The temperature in the PNe—in the interstellar medium in general—can vary significantly, from several tens to several thousands of Kelvin. Previously, using the thermal excitation model, Cami et al. derived a temperature range of 319–347 K for C_{60} and 142–243 K for C_{70} by fitting their observational band intensities in Tc 1 (Cami et al. 2010). To obtain a wide range of dependence on the temperature, we perform our calculations at two different temperatures of 50 and 300 K.

In space, the $[C_{60}\text{-Metal}]^+$ complexes can form via (i) $C_{60} + \text{Metal}^+$, (ii) $C_{60}^+ + \text{Metal}$, or (iii) $C_{60} + \text{Metal} + h\nu$ (photoionization). From k_{L1} ($C_{60} + \text{Metal}^+$) and k_{L2} ($C_{60}^+ + \text{Metal}$) in Table A2, it can be seen that the first two routes have comparable collision rate constants independent of temperature. Even ignoring the requirement of post-ultraviolet (UV) photoionization after forming the neutral $[C_{60}\text{-Metal}]$ complex, the neutral route (k_{HS} in Table A2) has collision rate constants about one order of magnitude lower than the two ionic routes. It is challenging to estimate the photoionization efficiency for forming the $[C_{60}\text{-Metal}]^+$ complexes via the neutral route as it depends on both the radiation flux and the photoionization cross sections of neutral $[C_{60}\text{-Metal}]$, which are unknown. The abundances of Metal^+ ions are also challenging to quantify. Hence, we simplify the problem by considering only the $C_{60} + \text{Metal}$ route to estimate a lower limit of the $[C_{60}\text{-Metal}]^+$ formation rate using k_{L2} , which is in the range of $1–4 \times 10^{-9} \text{ cm}^3 \cdot \text{s}^{-1}$ depending on the specific metals (Table A2). Hence, the formation rate of $[C_{60}\text{-Metal}]^+$ complexes per C_{60}^+ molecule is in the range of $\sim(1.5 \times 10^{-19}–6.3 \times 10^{-14}) \cdot n_H \text{ cm}^3 \cdot \text{s}^{-1}$. Using a previously quoted value of $n_H < 2 \times 10^4 \text{ cm}^{-3}$ by Omont in estimating the formation of $C_{60}\text{H}^+$ (Omont 2016), the $[C_{60}\text{-Metal}]^+$ formation rate is estimated to be $< 3 \times 10^{-15}–1.2 \times 10^{-9} \text{ s}^{-1}$ (or $< 1 \times 10^{-7}–4 \times 10^{-2} \text{ yr}^{-1}$) per C_{60}^+ molecule (Table A2).

The C_{60} fullerene has a longer lifetime than the few 10^8 yr estimated lifetime of PAHs, from which it is thought to form

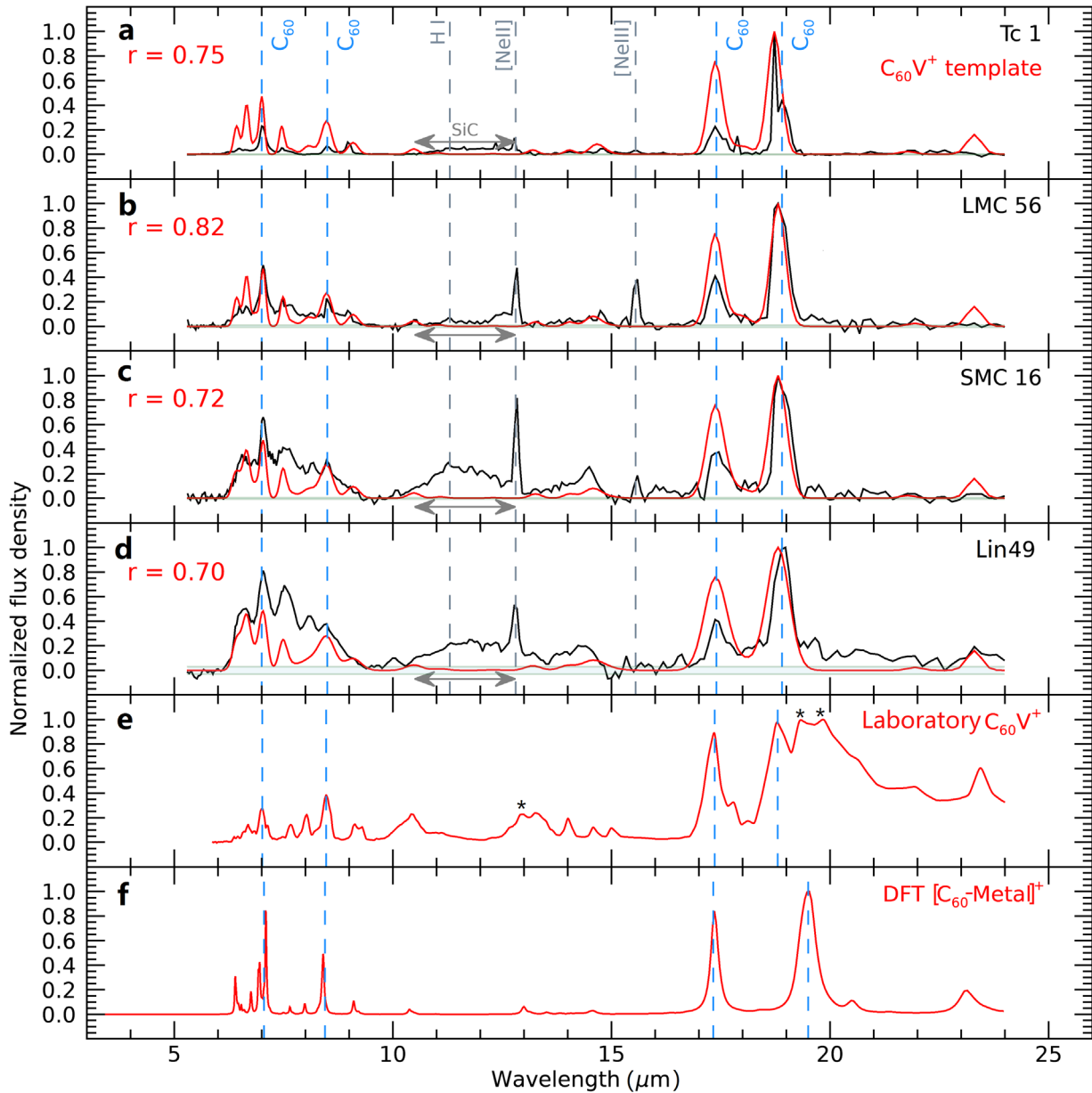


Figure A4. Comparison between the Spitzer infrared spectra of four fullerene-rich PNe (black) and the $C_{60}V^+$ template constructed by scaling the laboratory $C_{60}V^+$ spectrum to the DFT-calculated band intensities (red). (a) Tc 1, (b) LMC 56, (c) SMC 16, (d) Lin 49. The spectra of Tc 1, LMC 56 and SMC 16, and Lin 49 are adapted from Cami et al. (2010), Bernard-Salas et al. (2012), and Otsuka et al. (2016). The cross-correlation coefficients of the observational PN spectrum and the $C_{60}V^+$ template are indicated in each panel. The thickness of the horizontal, light gray line indicates the 3σ detection limit (see Details on the Astronomical Data section of the Appendix). (e) Laboratory infrared spectrum of $C_{60}V^+$. The asterisks indicate D_2 -tag induced bands, hence without possible UIE counterparts. (f) Summed theoretical spectrum of $[C_{60}\text{-Metal}]^+$. See the caption of Figure 2 for more details.

(Micelotta et al. 2010). In evolved stars (Table A1), around 1% of cosmic carbon is estimated to be locked in C_{60}^+ , and the carbon abundance (Table A4) is about $(1.6\text{--}3.8 \times 10^{-4}) \cdot n_{\text{H}}$, which gives a number density of C_{60}^+ around $0.05\text{--}0.13 \text{ cm}^{-3}$ for $n_{\text{H}} < 2 \times 10^4 \text{ cm}^{-3}$ and an estimated formation rate of $[C_{60}\text{-Metal}]^+$ complexes to be $5 \times 10^{-9}\text{--}5.2 \times 10^{-3} \text{ cm}^{-3} \text{ yr}^{-1}$.

We note that this estimated formation rate may underestimate their abundance in space because it assumes that the fullerenes already form and undergo random collisions with metal atoms to form the complexes. It is well-recognized that metals can catalyze the nucleation and growth of various carbon nanostructures, including carbon nanotubes (Esconjauregui et al. 2009) and carbon cages even under oxygen- and hydrogen-rich conditions (Dunk et al. 2013,

2014). We therefore conjecture that metals could play a role in the initial steps of forming various carbonaceous species including carbon cages and their complexes, enhancing their abundances in space. This mechanism can potentially link the chemical pathways and mechanisms of the formation and evolution of various carbonaceous species. For example, Ziurys and coworkers recently found that C_{60} could form from the decomposition of SiC dust grains under relevant interstellar conditions (Bernal et al. 2019). It is known that SiC grains are commonly associated with the objects where C_{60} has been identified and that they contain various metals (Cami et al. 2010; Bernard-Salas et al. 2012; Otsuka et al. 2016; Bernal et al. 2019), making it plausible that the presence of metals could facilitate the decomposition of

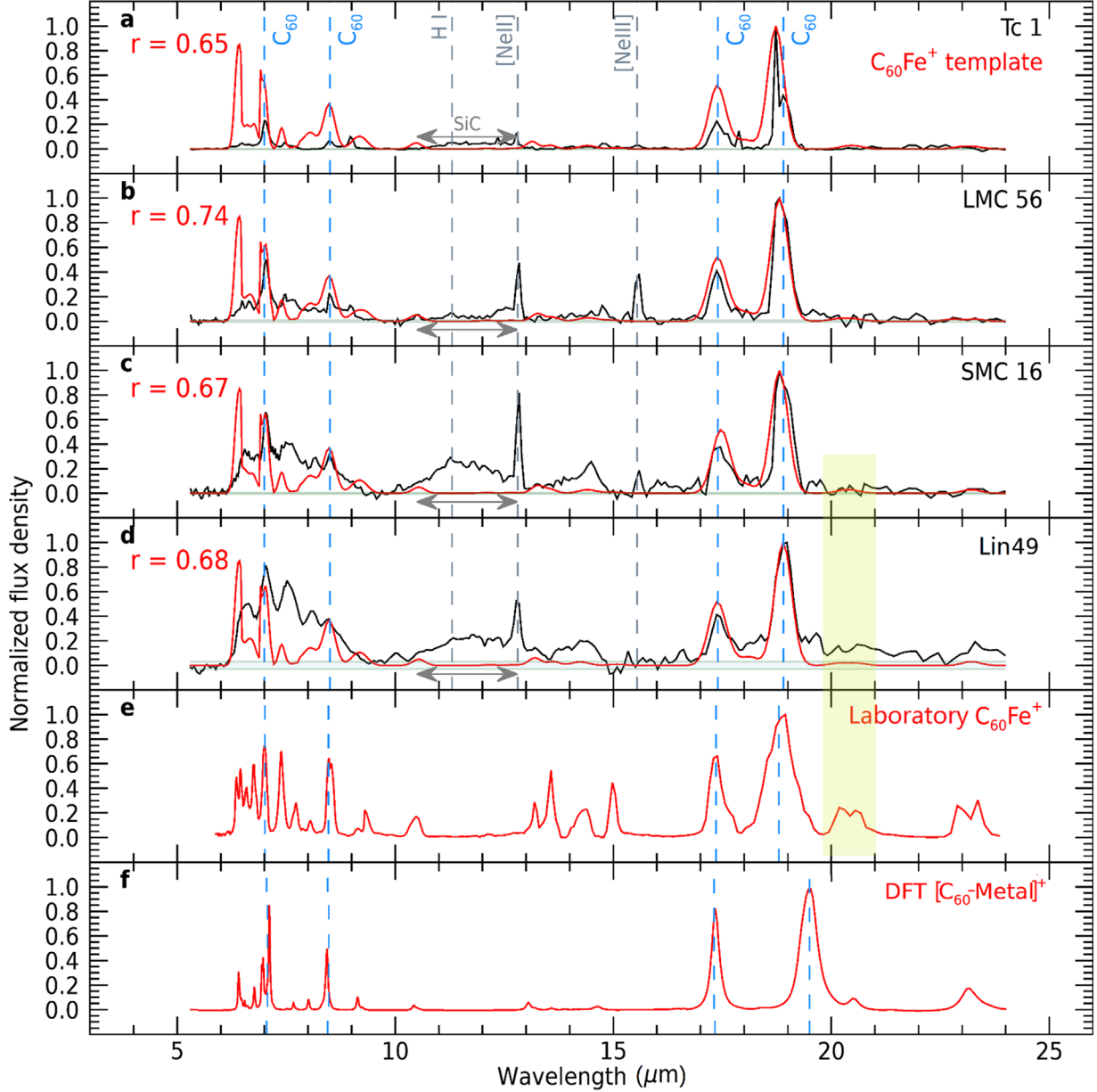


Figure A5. Comparison between the Spitzer infrared spectra of four fullerene-rich PNe (black) and the $C_{60}Fe^+$ template constructed by scaling the laboratory $C_{60}Fe^+$ spectrum to the DFT-calculated band intensities (red). (a) Tc 1, (b) LMC 56, (c) SMC 16, (d) Lin 49. The spectra of Tc 1, LMC 56 and SMC 16, and Lin 49 are adapted from Cami et al. (2010), Bernard-Salas et al. (2012), and Otsuka et al. (2016). The cross-correlation coefficients of the observational PN spectrum and the $C_{60}Fe^+$ template are indicated in each panel. The thickness of the horizontal, light gray line indicates the 3σ detection limit (see Details on the Astronomical Data section of the Appendix). (e) Laboratory infrared spectrum of $C_{60}Fe^+$. (f) Summed theoretical spectrum of $[C_{60}\text{-Metal}]^+$. See the caption of Figure 2 for more details.

SiC and the formation of carbon cages, consistent with previous findings (Dunk et al. 2013). This potential formation pathway involving metals may help explain the abundance of C_{60} in hydrogen-rich environments and could greatly enhance the abundance of fullerene-metal complexes in space, representing an interesting mechanism deserving further investigation in laboratory simulated astrophysical conditions.

Thermal Dissociation Rates of the $[C_{60}\text{-Metal}]^+$ Complexes. We approximate the unimolecular thermal dissociation rate (k_d) of the $[C_{60}\text{-Metal}]^+$ complex with an Arrhenius form,

$$k_d = A \cdot \exp\left(\frac{-E_a}{RT}\right), \quad (11)$$

where A is the prefactor, R is the ideal gas constant, T the temperature of the complex, and E_a the activation energy for which we use the calculated $[C_{60}\text{-Metal}]^+$ binding energy. To have a nonzero dissociation rate, the internal energy should be much higher than the activation energy (or binding energy) due to the intramolecular energy redistribution and the finite heat capacity of the complex. For example, the dominant dissociation channel of $C_{60} \rightarrow C_2 + C_{58}$ has an activation energy of 10.8 ± 0.3 eV, but internal energies of about 50 eV are needed for dissociation on a timescale of tens to hundreds of microseconds (Tomita et al. 2003). Considering the similar binding strength and the same size of $C_{60}C^+$ with $[C_{60}\text{-Metal}]^+$, we here take the prefactor $A = 1.6 \times 10^{15} s^{-1}$ determined previously for $C_{60}C^+$ to estimate their thermal

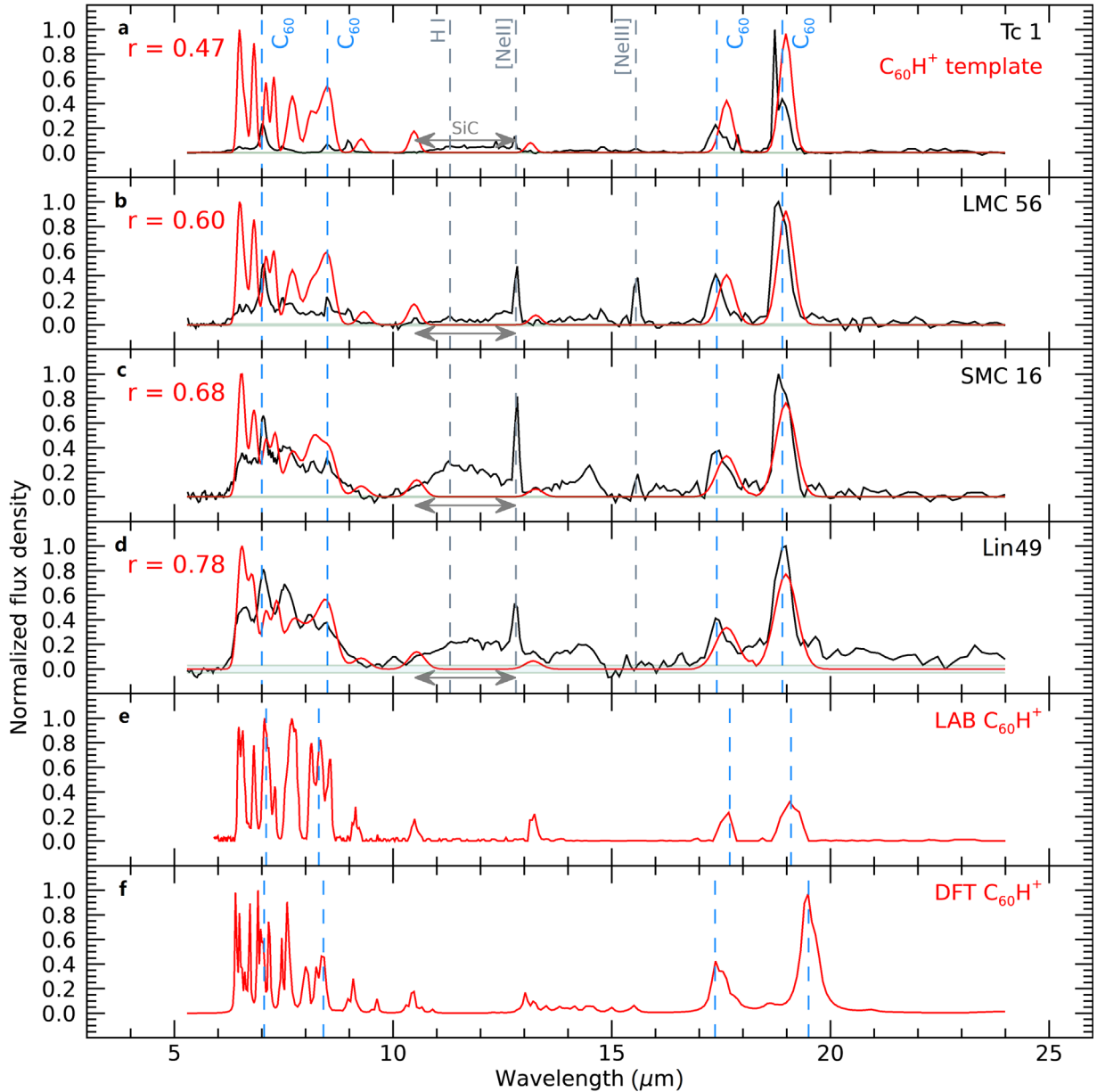


Figure A6. Comparison between the Spitzer infrared spectra of four fullerene-rich PNe (in black) and the C_60H^+ template constructed by scaling laboratory C_60H^+ spectrum to the DFT-calculated intensities (in red). (a) Tc 1, (b) LMC 56, (c) SMC 16, (d) Lin 49. The spectra of Tc 1, LMC 56 and SMC 16, and Lin 49 are adapted from Cami et al. (2010), Bernard-Salas et al. (2012), and Otsuka et al. (2016). The cross-correlation coefficients of the observational PN spectrum and the C_60H^+ template are indicated in each panel. The thickness of the horizontal, light gray line indicates the 3σ detection limit (see Details on the Astronomical Data section of the Appendix). (e) Laboratory infrared spectrum of C_60H^+ (Palotás et al. 2020). (f) BPW91/6-31G(d)-calculated spectrum of C_60H^+ . See the caption of Figure 2 for more details.

dissociation rates (Klots 1991; Berné et al. 2015). In Table A2, we summarize the thermal dissociation rates at two temperatures of 50 and 300 K.

Photodissociation Rates of the $[\text{C}_60\text{-Metal}]^+$ Complexes. The complexes can also be destroyed by collision-induced dissociation or UV photodissociation. Collision-induced dissociation is not important due to the high binding energies of the complexes and the relatively low collision energies given the generally low temperature of the environment. The rate of UV photodissociation is challenging to estimate.

UV photodissociation implies dissociation of $[\text{C}_60\text{-Metal}]^+$ following the absorption of a UV photon. Since the photoabsorption rate is much lower than the vibrational cooling rate (see below), the sequential absorption of UV photons can

be ignored. Under these conditions, the UV photodissociation rate (k_{PD}) can be approximated by the product of the photoabsorption rate (k_{PA}) with the probability that the complex will dissociate if a single UV photon is absorbed (p_d).

Only photons with an energy between 6 and 9 eV are considered relevant since competing decay rates are much higher than dissociation rates if the complex has internal energies below 6 eV (see below) and photoionization (to higher charge states) dominates upon absorption of photons with energies above 9 eV. The calculated ionization energies of $[\text{C}_60\text{-Metal}]^+$ (8.65, 8.95, and 9.04 eV for Ca, Fe, and V, respectively) are much lower than that of C_60^+ (18.98 ± 0.35 eV) (Pogulay et al. 2004). The typical timescale for photoionization, an electronic process, is much shorter than that

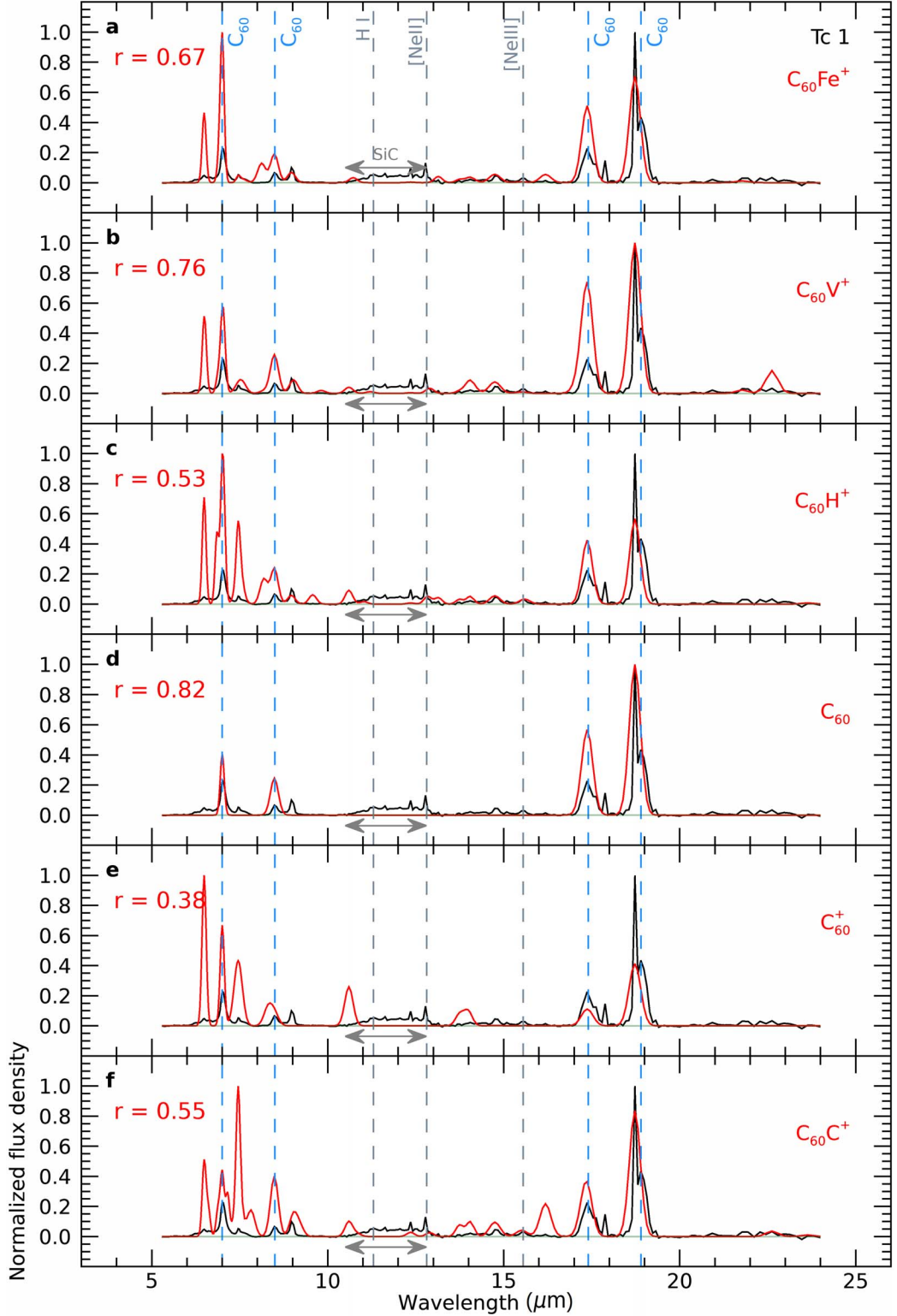


Figure A7. Comparison between the Spitzer infrared spectrum of Tc 1 (in black) and the DFT-calculated spectra (in red). (a) C_{60}Fe^+ , (b) C_{60}V^+ , (c) C_{60}H^+ , (d) C_{60} , (e) C_{60}^+ , and (f) C_{60}C^+ . The cross-correlation coefficients of the observational spectrum and the C_{60} -related species are indicated in each panel. The blue dashed lines indicate the four C_{60} bands; gray dashed lines some of the strong atomic emission lines, for example, [Ne II] ($12.81 \mu\text{m}$) and [Ne III] ($15.55 \mu\text{m}$) (Cami et al. 2010). The thickness of the horizontal, light gray line indicates the 3σ detection limit (see Details on the Astronomical Data section of the Appendix). See the caption of Figure 2 for more details.

of dissociation, which involves atomic motion. In a Habing field, there are of the order of $10^8 \text{ photons cm}^{-2} \text{ s}^{-1}$ between 6 and 9 eV (Tielens 2005). The C_{60} photoabsorption cross section in this photon energy range is about 200 Mb

($1 \text{ Mb} = 1 \times 10^{-18} \text{ cm}^2$) (Berkowitz 1999), which yields a k_{PA} on the order of $2 \times 10^{-8} \text{ s}^{-1}$. In the photodissociation region (PDR), the number of photons can be a factor of 10^4 higher, which yields an upper limit for k_{PA} of 10^{-4} s^{-1} .

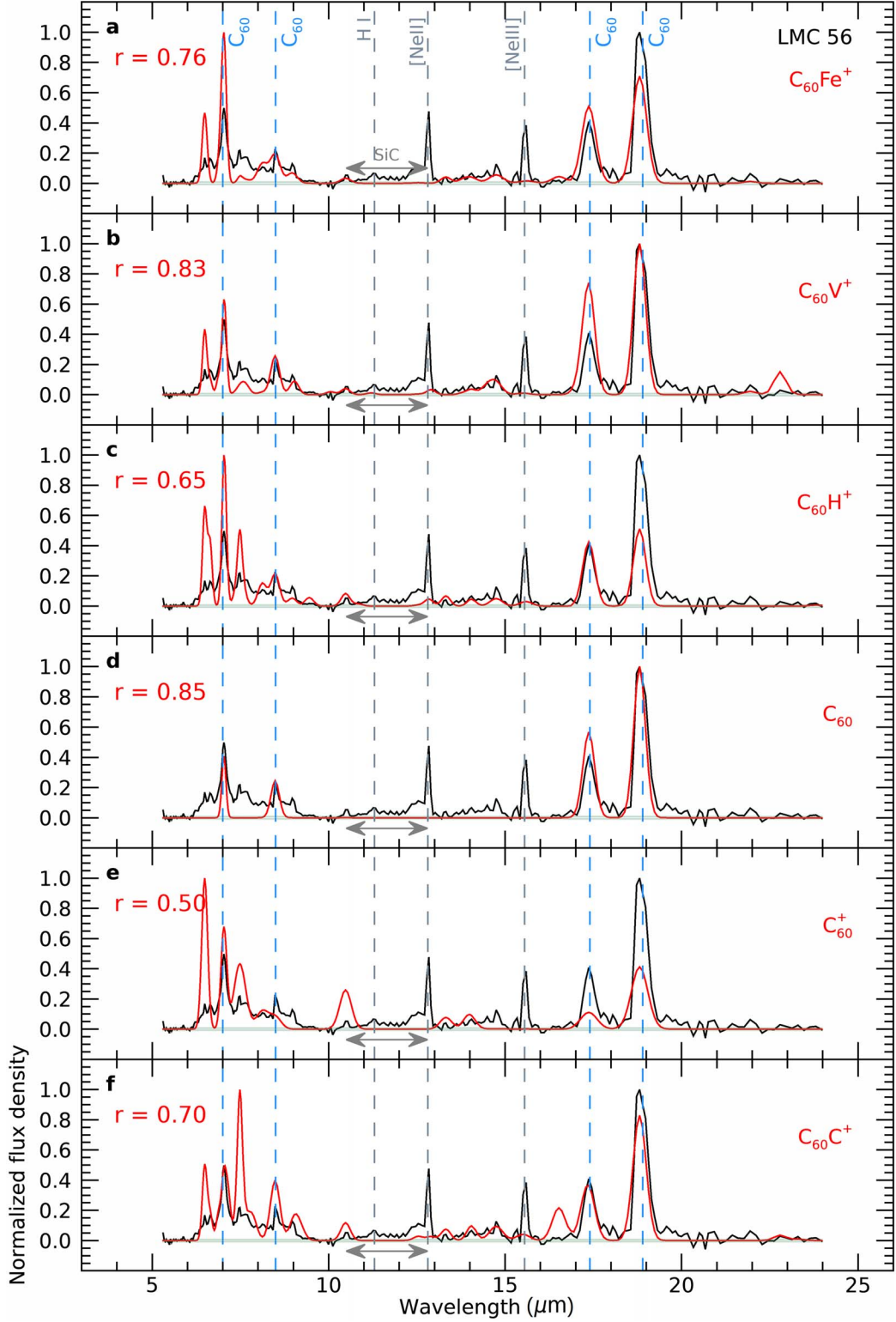


Figure A8. Comparison between the Spitzer infrared spectrum of LMC 56 (in black) and the DFT-calculated spectra (in red). (a) C_{60}V^+ , (b) C_{60}V^+ , (c) C_{60}H^+ , (d) C_{60} , (e) C_{60}^+ , and (f) C_{60}C^+ . The cross-correlation coefficients of the observational spectrum and the C_{60} -related species are indicated in each panel. The blue dashed lines indicate the four C_{60} bands and the gray dashed lines some of the strong atomic emission lines, for example, [Ne II] ($12.81 \mu\text{m}$) and [Ne III] ($15.55 \mu\text{m}$) (Cami et al. 2010). The thickness of the horizontal, light gray line indicates the 3σ detection limit (see Details on the Astronomical Data section of the Appendix). See the caption of Figure 2 for more details.

Once a UV photon is absorbed and the internal energy of $[\text{C}_{60}\text{-Metal}]^+$ is higher than its binding energy, the complex can dissociate. The rate will, however, strongly depend on the internal energy, the density of states, the dissociation

pathway, and the dissociation threshold of the complex. In earlier work, with a statistical model provided for C_{60}H_2 , which has a binding energy of 2.9 eV comparable to that of C_{60}V^+ , the dissociation rate k_d was estimated to be on the

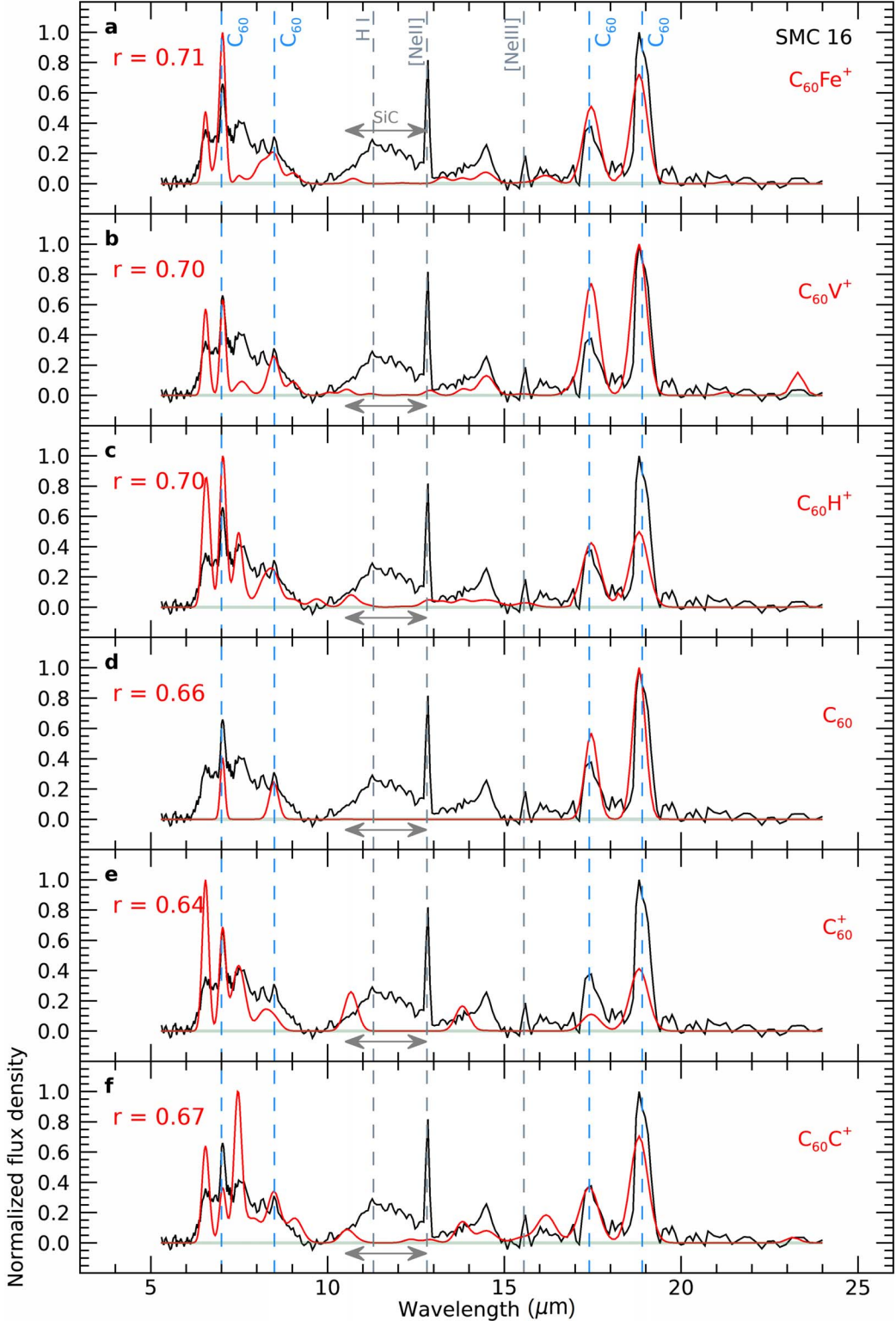


Figure A9. Comparison between the Spitzer infrared spectrum of SMC 16 (in black) and the DFT-calculated spectra (in red). (a) C_{60}Fe^+ , (b) C_{60}V^+ , (c) C_{60}H^+ , (d) C_{60} , (e) C_{60}^+ , and (f) C_{60}C^+ . The cross-correlation coefficients of the observational spectrum and the C_{60} -related species are indicated in each panel. The blue dashed lines indicate the four C_{60} bands and the gray dashed lines some of the strong atomic emission lines, for example, [Ne II] ($12.81 \mu\text{m}$) and [Ne III] ($15.55 \mu\text{m}$) (Cami et al. 2010). The thickness of the horizontal, light gray line indicates the 3σ detection limit (see Details on the Astronomical Data section of the Appendix). See the caption of Figure 2 for more details.

order of 10^{-5} – 10^{-1} s^{-1} following absorption of a photon between 6 and 9 eV (Tielens 2005). For C_{60}V^+ , this rate is likely lower considering that the dissociation coordinate ($\text{V}-\text{C}_{60}$ cage stretching vibration; $\sim 430 \text{ cm}^{-1}$) of C_{60}V^+ has a

much lower frequency than that of C_{60}H_2 ($\text{H}-\text{C}_{60}$ cage stretching vibration; $\sim 2800 \text{ cm}^{-1}$).

The dissociation process competes with other decay channels, greatly affecting the dissociation probability. The

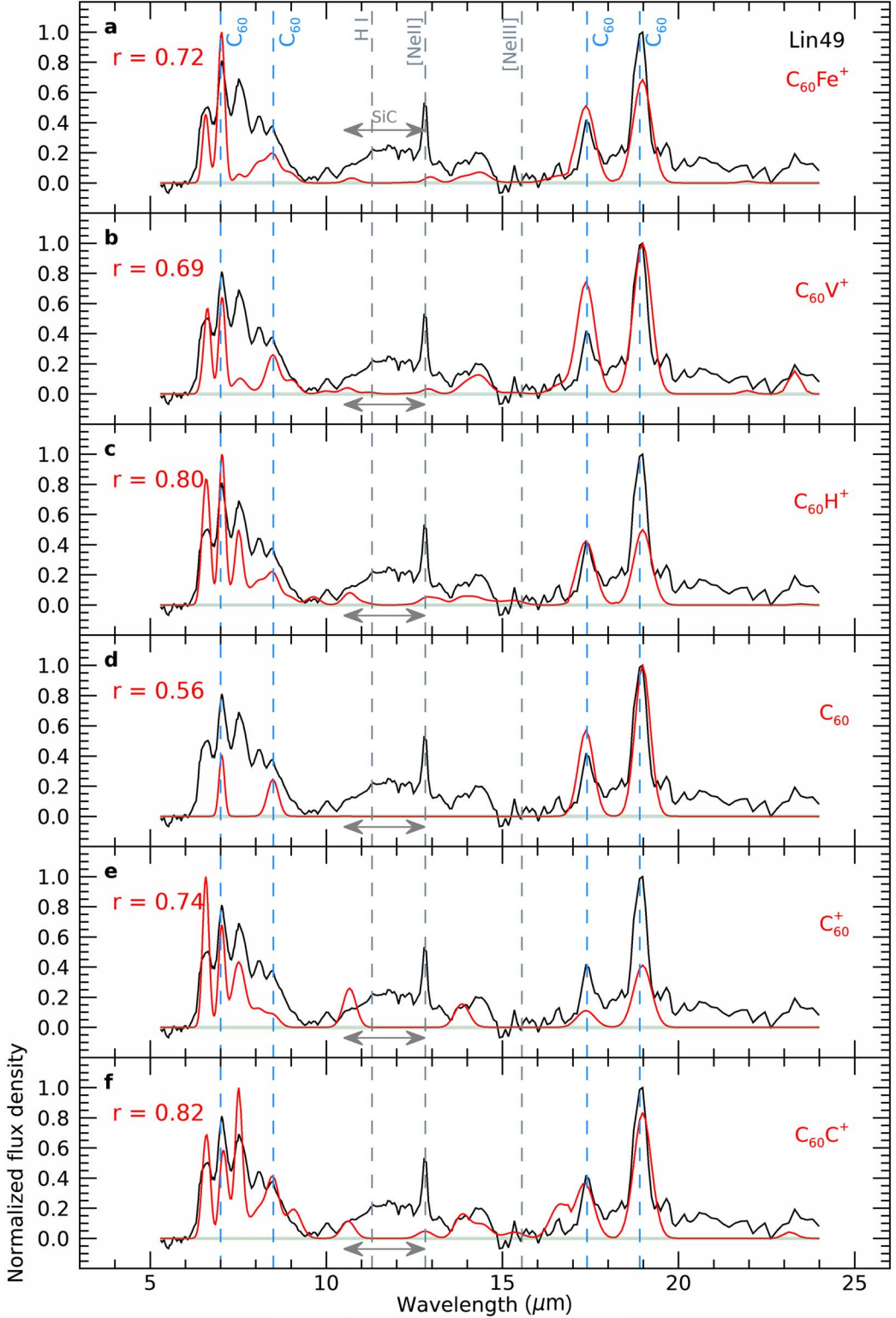


Figure A10. Comparison between the Spitzer infrared spectrum of Lin 49 (in black) and the DFT-calculated spectra (in red). (a) C_{60}Fe^+ , (b) C_{60}V^+ , (c) C_{60}H^+ , (d) C_{60} , (e) C_{60}^+ , and (f) C_{60}C^+ . The cross-correlation coefficients of the observational spectrum and the C_{60} -related species are indicated in each panel. The blue dashed lines indicate the four C_{60} bands and the gray dashed lines some of the strong atomic emission lines, for example, [Ne II] ($12.81 \mu\text{m}$) and [Ne III] ($15.55 \mu\text{m}$) (Cami et al. 2010). The thickness of the horizontal, light gray line indicates the 3σ detection limit (see Details on the Astronomical Data section of the Appendix). See the caption of Figure 2 for more details.

two most important competing decay channels are (i) de-excitation via vibrational cooling and infrared emission and (ii) de-excitation via recurrent fluorescence, which is likely important since $[\text{C}_{60}\text{-Metal}]^+$ has a dense spectrum of low-

energy electronic transitions (Figure A13). The thermal population of low-energy electronic excited states leads to photon emission, the so-called recurrent fluorescence, thereby cooling $[\text{C}_{60}\text{-Metal}]^+$ (Ferrari et al. 2019). Taking into account

Table A2
Collision Constant and Thermal Dissociation Rate of $[C_{60}\text{-Metal}]^+$ Complexes

Metals	Radius ^a (Å)	Polarizability ^b (\AA^3)	Binding Energy (eV)	Collision Rate Constant ^c (10^{-9} $\text{cm}^3 \cdot \text{s}^{-1}$)			Formation Rate ^d (s^{-1} per C_{60}^+)		Thermal Dissociation Rate ^e (s^{-1})	
				k_{HS}		k_{L1}	k_{L2}	Sol	IS	k_d
				50 K	300 K					50 K
V	1.71	12.9	2.82	0.22	0.54	3.03	1.22	2.45×10^{-13}	3.10×10^{-15}	0
Li	1.67	24.3	1.55	0.57	1.40	7.95	4.38	1.75×10^{-13}	4.40×10^{-15}	0
Na	1.86	24.1	1.05	0.34	0.82	4.43	2.43	9.70×10^{-11}	1.23×10^{-11}	0
K	2.43	42.9	0.67	0.31	0.75	3.44	2.52	6.35×10^{-12}	5.05×10^{-13}	0
Mg	1.45	10.6	1.07	0.29	0.71	4.34	1.58	1.25×10^{-9}	3.16×10^{-11}	0
Ca	1.94	23.8	1.07	0.26	0.65	3.40	1.85	7.40×10^{-11}	1.48×10^{-14}	0
Al	1.18	8.6	1.69	0.25	0.62	4.10	1.35	6.76×10^{-11}	3.40×10^{-13}	0
Fe	1.56	9.2	2.25	0.20	0.49	2.90	0.98	6.23×10^{-10}	3.10×10^{-12}	0

Notes.

^a The atomic radii are from: [https://en.wikipedia.org/wiki/Atomic_radii_of_the_elements_\(data_page\)](https://en.wikipedia.org/wiki/Atomic_radii_of_the_elements_(data_page)).

^b The polarizabilities are from Schwerdtfeger & Nagle (2019).

^c k_{HS} is the collision rate constant for the neutral route $C_{60} + \text{Metal}$, and k_{L1} and k_{L2} are for $C_{60} + \text{Metal}^+$ and $C_{60}^+ + \text{Metal}$ routes, respectively.

^d The formation rates of $[C_{60}\text{-Metal}]^+$ complexes via the $C_{60}^+ + \text{Metal}$ route for a single C_{60}^+ molecule based on the solar and interstellar metal abundances, respectively (Table A4).

^e The universe has an estimated age of 13.8 billion years (Planck Collaboration et al. 2016); therefore, we define dissociation rates lower than the age of universe, i.e., 1.38×10^{10} yr or 4.35×10^{17} s, to be zero.

Table A3

The Relative Stabilities (in kJ mol^{-1}) and Average V–C Distances (in Angstroms) of the Different Structures of $C_{60}\text{V}^+$ in Different Spin States at Three Different Levels of Theory, i.e., BPW91, PBE, and B3LYP

		BPW91/6-31G(d)		PBE/def2-SVP		B3LYP/def2-SVP	
		ΔE	V–C	ΔE	V–C	ΔE	V–C
η^5	$S = 0$	128.0	2.140	140.2	2.153	164.5	2.243
	$S = 1$	46.9	2.250	46.4	2.267	67.0	2.328
	$S = 2$	0.0	2.282	0.0	2.306	0.0	2.416
η^6	$S = 0$	138.0	2.220	145.7	2.229	157.8	2.350
	$S = 1$	39.3	2.246	41.3	2.263	51.4	2.585
	$S = 2$	7.5	2.358	11.5	2.419	0.9	2.510
$\eta^{2(6-6)}$	$S = 0$	207.8	1.912	$\rightarrow\eta^6$		177.2	2.056
	$S = 1$	$\rightarrow\eta^6$		$\rightarrow\eta^6$		55.1	2.078
	$S = 2$	31.4	2.181	33.5	2.202	3.59	2.290
$\eta^{2(6-5)}$	$S = 0$	$\rightarrow\eta^6$		$\rightarrow\eta^6$		$\rightarrow\eta^6$	
	$S = 1$	91.5	2.077	$\rightarrow\eta^5$		54.5	2.068
	$S = 2$	35.4	2.174	40.5	2.189	$\rightarrow\eta^6$	

Note. For certain isomer and theory level combinations, the optimization converged to more stable isomers as indicated.

Table A4
Abundance of Metal Elements Studied in This Work

Metals	Sol ^a	IS ^a	RedRec ^b
H	0	0	0
C	-3.5	-3.8	-3.34
V	-8.0	-9.9	...
Li	-8.7	-10.3	...
Na	-5.7	-6.6	...
K	-6.9	-8.0	...
Mg	-4.4	-6.0	-6.49
Ca	-5.7	-9.4	-8.75
Al	-5.6	-7.9	...
Fe	-4.5	-6.8	-7.82

Notes. They are provided by the logarithm ratios of metals relative to the abundance of atomic hydrogen, i.e., $\lg(n_{\text{metal}}/n_{\text{H}})$.

^a Solar and typical cool gas-phase interstellar abundances. From Jenkins (2009) and Savage & Sembach (1996).

^b Photospheric abundances in the Red Rectangle. From Waelkens et al. (1992).

the competing channels, the probability that the excited complex decays by dissociation is

$$p_d = \frac{k_d}{k_d + k_{VC} + k_{RF}}, \quad (12)$$

where k_d is the dissociation rate as noted above, k_{VC} is the vibrational cooling rate which has a typical value of $10\text{--}100 \text{ s}^{-1}$, and k_{RF} is the rate of recurrent fluorescence from electronic excited states, the value of which is not known but typical values of $10^4\text{--}10^5 \text{ s}^{-1}$ are found for metal, carbon or carbon-containing clusters (Ferrari et al. 2019). That gives a value for p_d on the order of $10^{-10}\text{--}10^{-5}$.

Combining the photoabsorption rate in the 6–9 eV range with the probability for dissociation, we obtain for the photodissociation rate $k_{PD} = k_{PA} \cdot p_d$ values on the order of

$10^{-14}\text{--}10^{-9} \text{ s}^{-1}$ or $10^{-6}\text{--}10^{-1} \text{ yr}^{-1}$, comparable to or slightly higher than the formation rate depending on different metals.

It should be noted that the photoabsorption cross section of $[\text{C}_60\text{-Metal}]^+$ is unknown and it can be different from that of C_60 . The arguments point out that conducting a more accurate estimate than the above on the photodissociation rates of $[\text{C}_60\text{-Metal}]^+$ complexes is currently not possible.

From Table A2, it can be seen that the formation rates for the complexes with Metal = V and Fe are significantly larger than their thermal dissociation rates. Hence, considering both the thermal dissociation rates and the current challenges for estimating the accurate photodissociation rates given the above arguments, it is plausible that the $[\text{C}_60\text{-Metal}]^+$ complexes could form and survive in certain astrophysical environments. In particular, the complexes with high binding energies such as C_60V^+ and C_60Fe^+ could be able to survive.

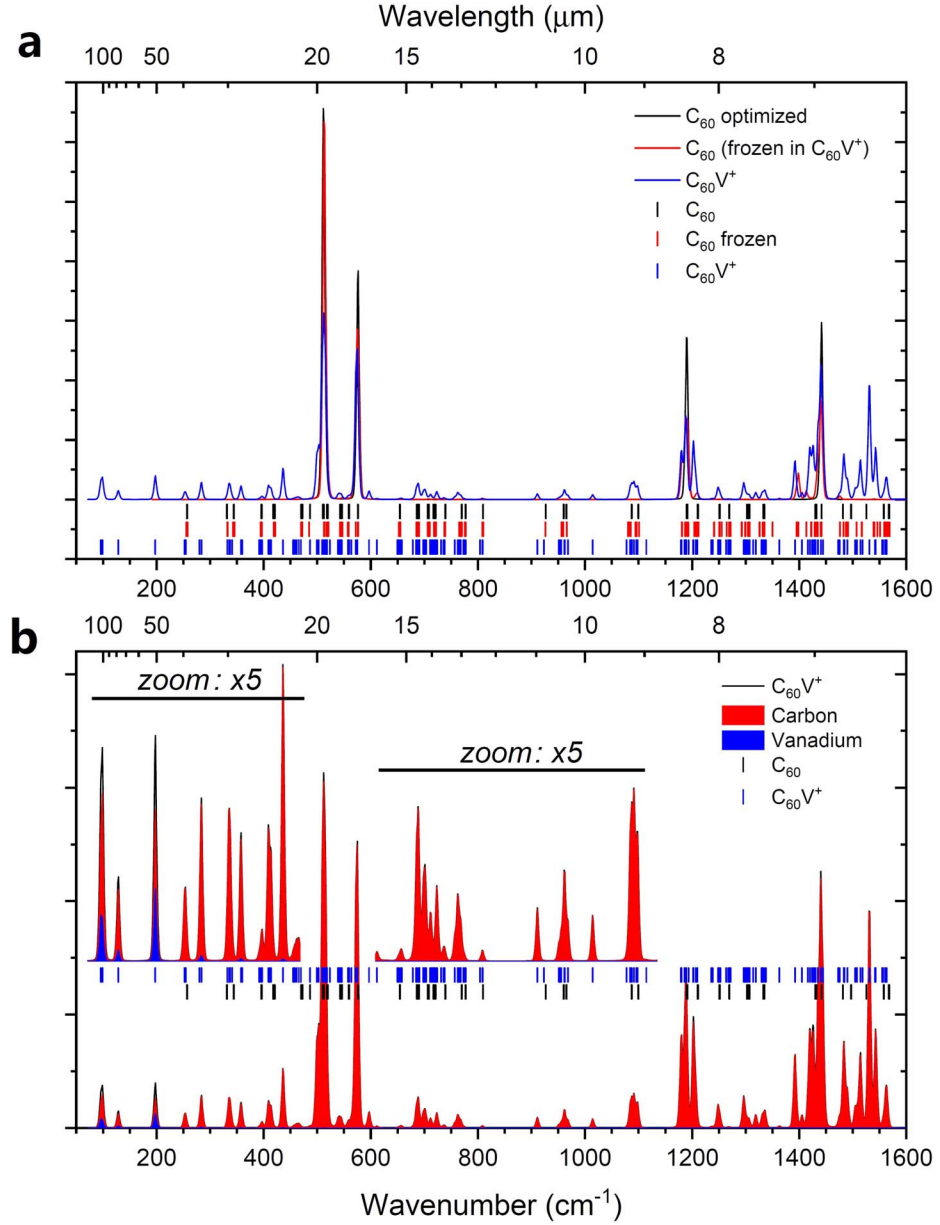


Figure A11. Influence of a metal atom on the vibrational property of C_{60} . (a) Vibrational spectra of the optimized icosahedral C_{60} (black line), the “frozen” C_{60} with the same geometry in C_{60}V^+ , where it is distorted by the V atom to a lower symmetry (red line), and C_{60}V^+ . The vibrational frequencies of all modes, including those carrying no infrared intensities, are displayed in sticks using the same color convention. It can be seen that the presence of a metal atom introduces much more infrared intensity than just lowering the C_{60} symmetry in addition to a few new vibrational modes. (b) Spectral decomposition of vibrational modes into motions involving the V atom (blue) and the carbon cage (red). These data represent the relative vector magnitudes of the V and C components of each normal mode displacement vector, projected onto the convolved infrared spectrum for C_{60}V^+ (Figure A11(a)). It can be seen that vibrational modes above 500 cm^{-1} (below $20 \mu\text{m}$) are dominated by C_{60} cage motions. Below 500 cm^{-1} (above $20 \mu\text{m}$), the V atom gets more involved, yielding metal-specific vibrational frequencies.

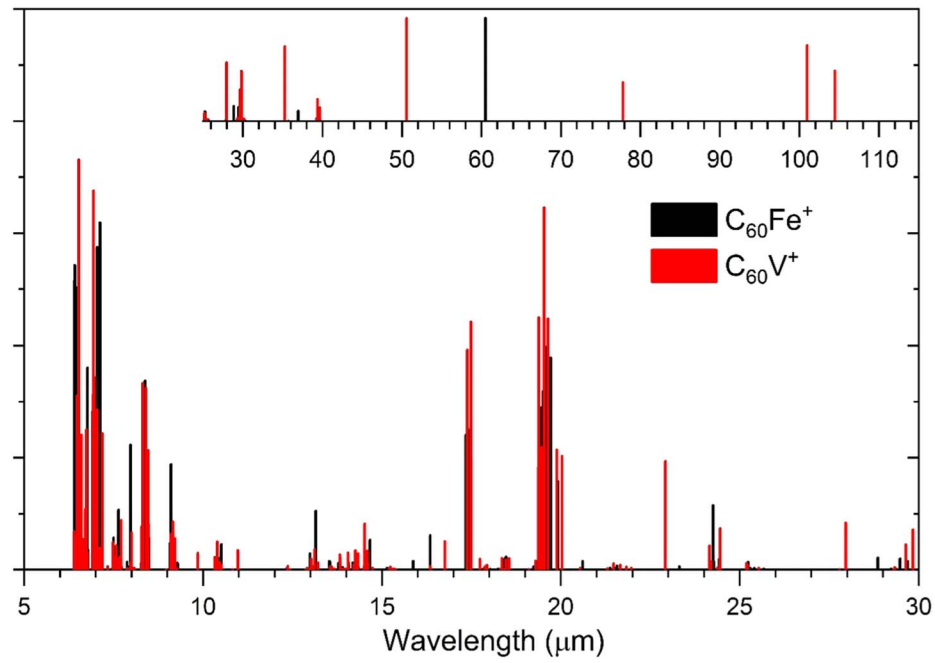


Figure A12. Detailed comparison of the predicted infrared spectra of $[C_{60}\text{-Metal}]^+$ (Metal = V, Fe). It demonstrates that the metal-specific vibrational bands start to emerge beyond $20\ \mu\text{m}$ and become more metal-dependent beyond $30\ \mu\text{m}$ as seen in Figure A3 as well.

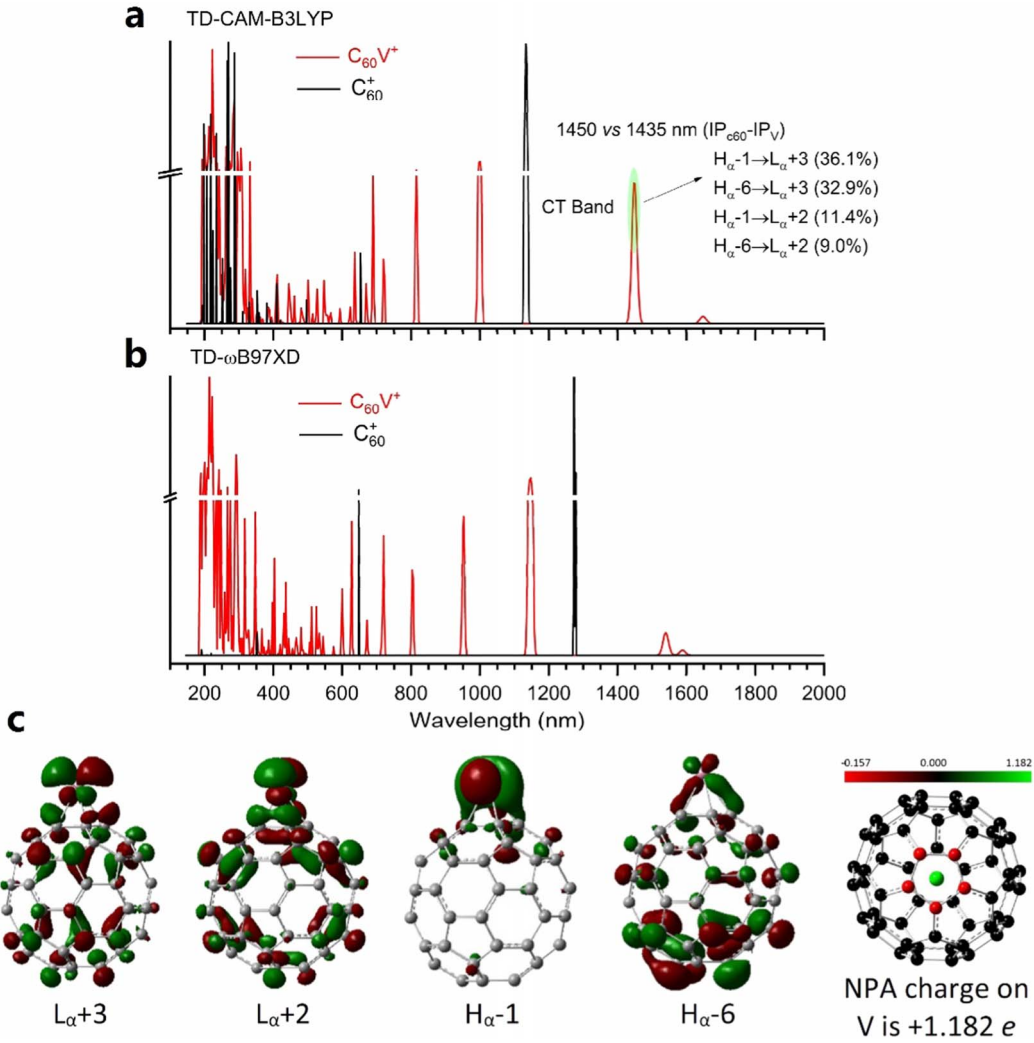


Figure A13. Simulated ultraviolet to visible to near-infrared (UV-Vis-NIR) absorption spectra of the most stable $C_{60}V^+$ using time-dependent density functional theory (TDDFT). The molecular orbitals (MOs) involved in the transition at 1450 nm (charge transfer from the metal to the C_{60} cage band, consistent with the charge distributions from natural population analysis (NPA)) are plotted. H_α represents the highest occupied MO with a spin-up electron, and L_α represents the lowest unoccupied MO with a spin-up electron. Kroto et al. have anticipated that the $[C_{60}\text{-Metal}]^+$ complexes should exhibit strong charge-transfer (CT) transitions with energies approximate to the ionization potential (IP) differences of C_{60} and metals (Kroto & Jura 1992). That will give a CT band for $C_{60}V^+$ at $(7.61 - 6.746 = 0.864$ eV) 1435 nm, close to the calculated CT band at 1450 nm (TD-CAM-B3LYP level of theory). The CT from the metal atom to the cage results in a strong C_{60} -metal interaction. The CAM-B3LYP functional comprises a 0.19 Hartree–Fock (HF) plus 0.81 Becke 1988 (B88) exchange interaction at short range and a 0.65 HF plus 0.35 B88 at long range. The intermediate region is smoothly described through the standard error function with parameter 0.33 (Yanai et al. 2004). The CAM-B3LYP functional has been shown to be superior to describe the charge-transfer excitation transitions (Jacquemin et al. 2008). The calculation using TD- ω B97XD is also carried out for comparison, and both functionals qualitatively show that the $C_{60}V^+$ complex has many more electronic transitions in 400–1000 nm compared to C_{60}^+ . Note that the quantitative prediction of the exact positions of those transitions is a huge challenge even for C_{60}^+ (Lykhin et al. 2018; Soler et al. 2019).

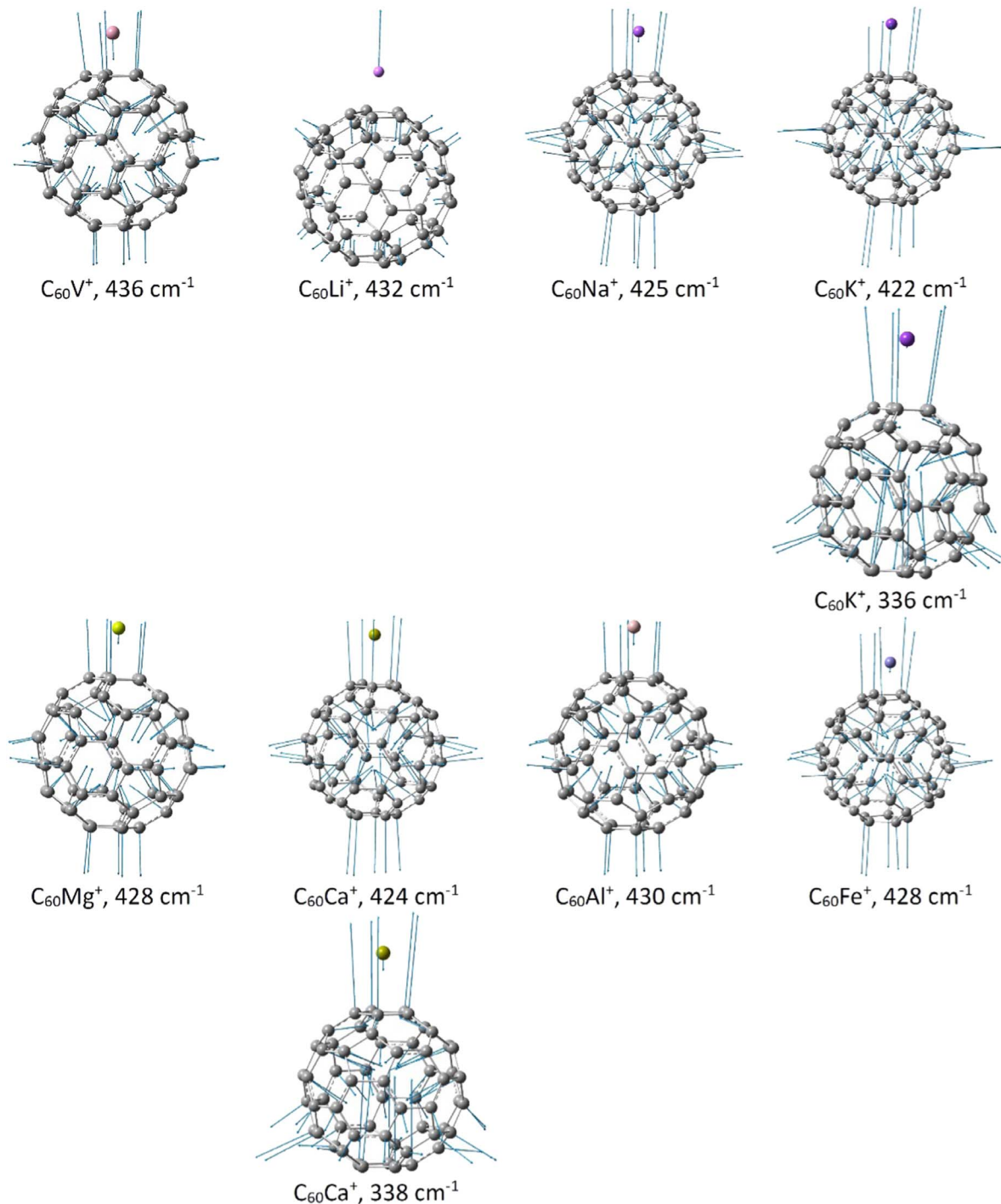


Figure A14. The vectors of the metal– C_{60} stretching modes of $[C_{60}\text{-Metal}]^+$ (Metal = V, Li, Na, K, Mg, Ca, Al, and Fe) and the calculated vibrational frequencies at the BPW91/6-31G(d) level of theory. Note that the $C_{60}\text{K}^+$ and $C_{60}\text{Ca}^+$ complexes have the metal– C_{60} stretching modes at lower frequencies ($\sim 340 \text{ cm}^{-1}$), while their modes around 430 cm^{-1} do not involve obvious movement of the metal atoms.

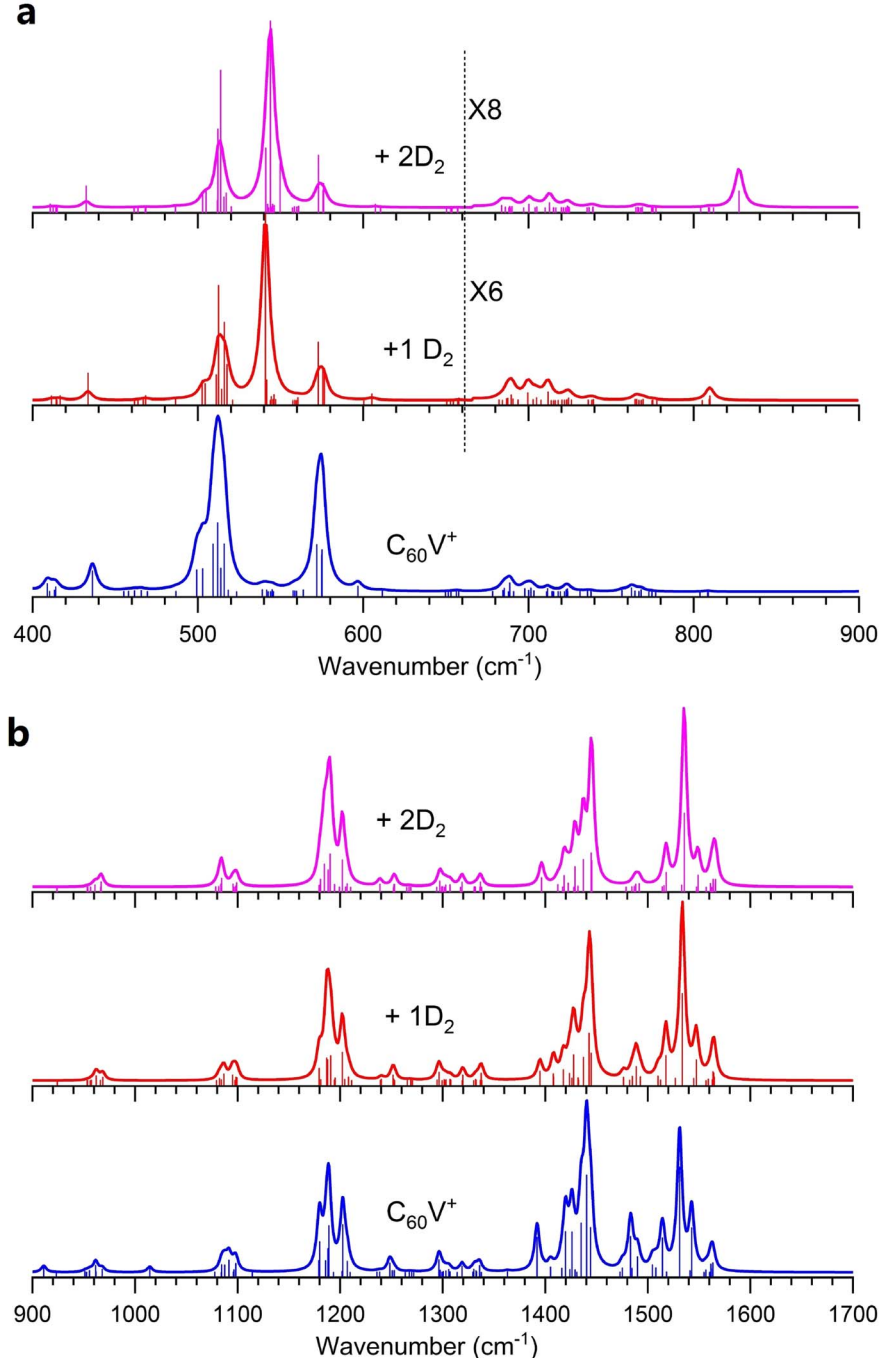


Figure A15. Simulated harmonic infrared spectra of $\text{C}_{60}\text{V}^+(\text{D}_2)_{0-2}$ with stick lines showing each infrared mode. The calculation is conducted at the BPW91/6-31G (d) level of theory, and the convolved spectra are using Lorentzian line shapes of 6 cm^{-1} FWHM. The convolved spectra of $\text{C}_{60}\text{V}^+(\text{D}_2)$ and $\text{C}_{60}\text{V}^+(\text{D}_2)_2$ in the $600\text{--}900 \text{ cm}^{-1}$ region are multiplied by factors of 6 and 8, respectively. It can be seen that the main visible changes caused by the D_2 tag are additional modes around $500\text{--}600$ and 830 cm^{-1} . There are many closely spaced vibrational modes in the $500\text{--}600 \text{ cm}^{-1}$ range calculated for $\text{C}_{60}\text{V}^+(\text{D}_2)_2$, being one factor contributing to the broadband features observed in experiment. The vectors of the vibrational modes that significantly involve D_2 motions are provided in Figure A16.

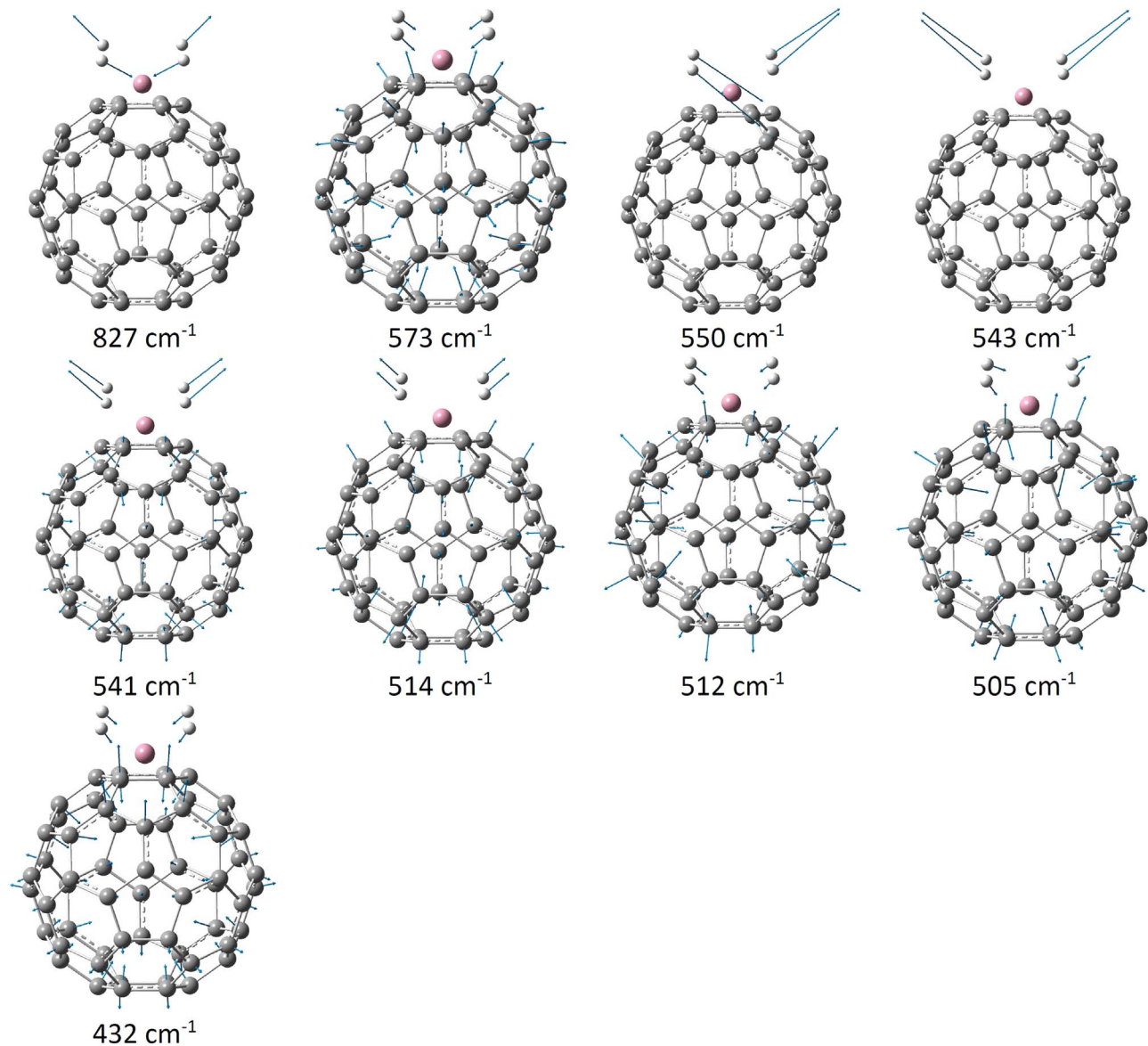


Figure A16. Vectors of the vibrational modes significantly involving the motions of D_2 molecules in the two D_2 -tagged C_{60}V^+ complex, i.e., $\text{C}_{60}\text{V}^+(\text{D}_2)_2$, and the calculated vibrational frequencies at the BPW91/6-31G(d) level of theory.

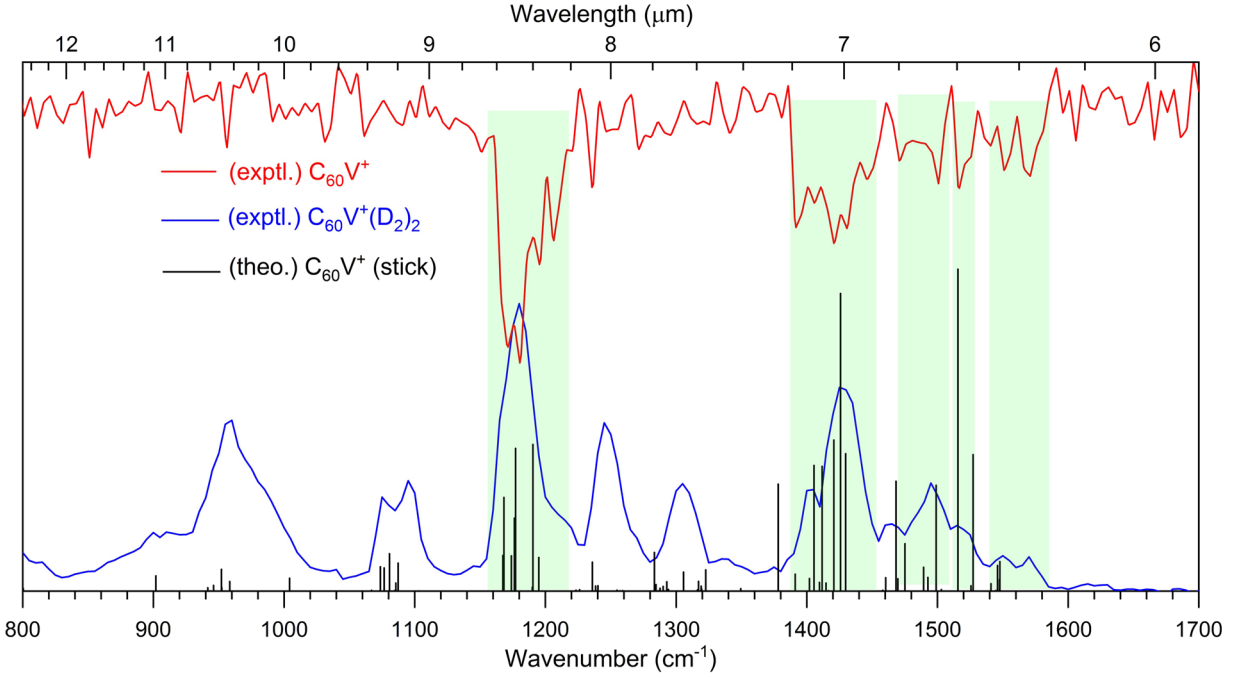


Figure A17. Laboratory IRMPD spectrum of C_{60}V^+ and its comparison with that of two D_2 -tagged C_{60}V^+ complexes and the DFT-simulated stick spectrum of the most stable C_{60}V^+ . The IRMPD spectrum of C_{60}V^+ was obtained without the D_2 tag. Hence, many photons are needed to induce the dissociation of $\text{C}_{60}\text{V}^+ \rightarrow \text{C}_{60} + \text{V}^+$ (the ionization potential of C_{60} is 7.61 eV and that of V is 6.746 eV; the dissociation energy is ca. 2.82 eV), and only the vibrational modes of high calculated infrared oscillator strengths were obtained. The features highlighted by green shading show that the D_2 tag almost does not alter the vibrational band positions of C_{60}V^+ . The vibrational modes with low calculated oscillator strengths were not observed for C_{60}V^+ since at those wavelengths not enough infrared photons can be absorbed to reach the dissociation threshold.

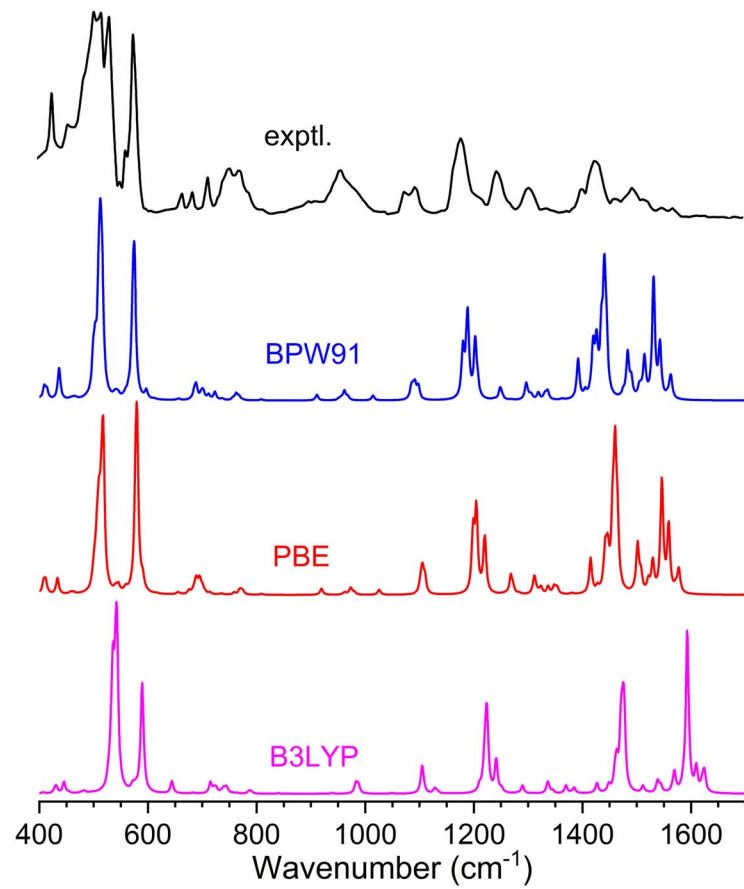


Figure A18. Simulated infrared spectra of the most stable C_{60}V^+ using three different functionals and their comparison with the experimental IRMPD spectrum. The simulated spectra are convolved using Lorentzian line shapes of 6 cm^{-1} FWHM. It can be seen overall the BPW91 functional provides the best agreement in comparison with experiment without applying any scaling factors.

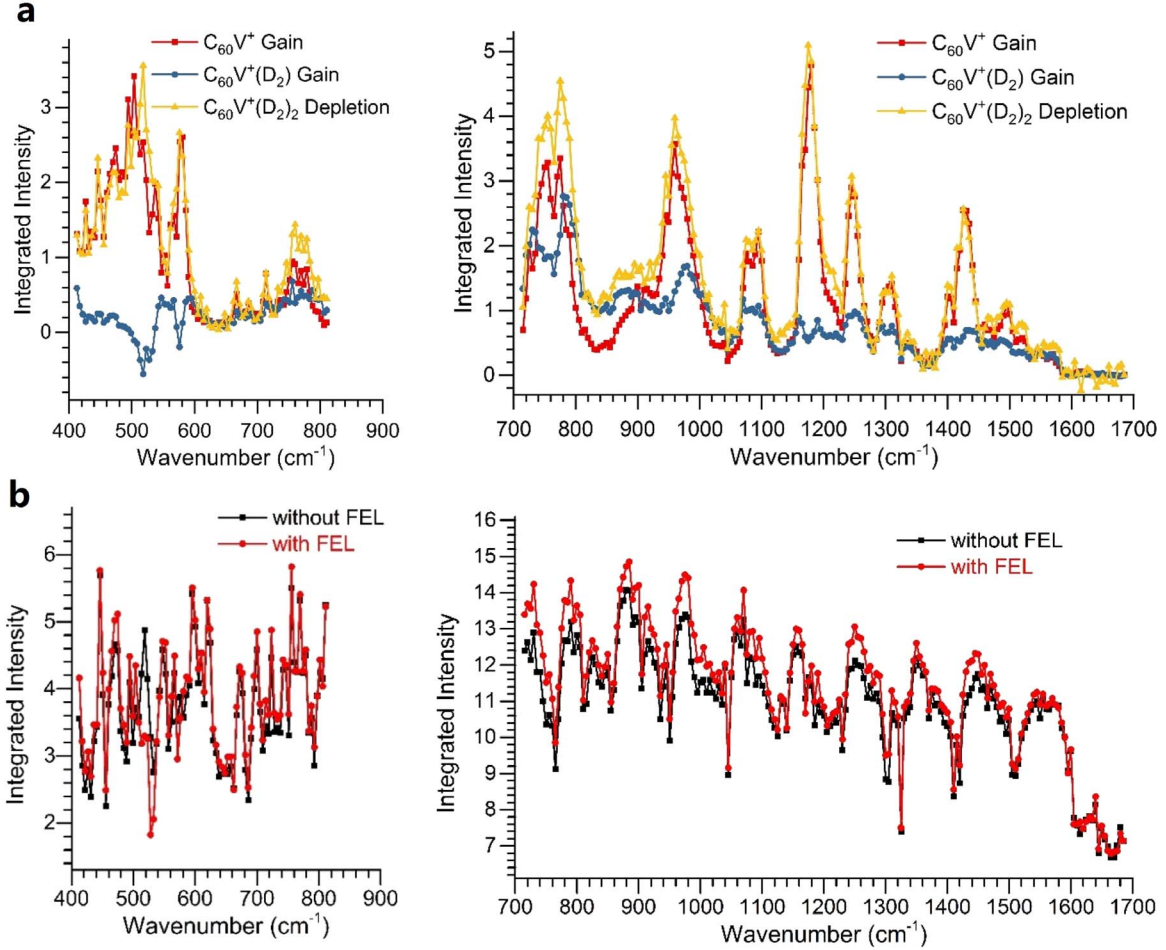


Figure A19. Integrated ion intensity as a function of infrared wavelength in the range of 400–1700 cm⁻¹. (a) The changes in the ion intensity of $C_{60}V^+$ and its D_2 -tagged complexes. (b) The total ion intensity of $C_{60}V^+$ and its D_2 -tagged complexes with (red) and without (black) FEL light irradiation. In general, it can be seen that both $C_{60}V^+$ and $C_{60}V^+(D_2)$ gain intensities from the depletion of $C_{60}V^+(D_2)_2$, except around 520 and 570 cm⁻¹, where $C_{60}V^+$ also gains a little intensity from the depletion of $C_{60}V^+(D_2)$. The comparison of the summed ion intensities with and without FEL shows that the total ion intensity is conserved within the experimental uncertainty, implying that there is no other dissociation channel than D_2 loss. Note that the experiments were performed with two separate FEL settings, covering the 400–850 and 700–1700 cm⁻¹ ranges. The quasi-repetitive fluctuation in the signal is attributed to the slight curvature in the target surface used for laser ablation, modulating the efficiency of the vaporization process.

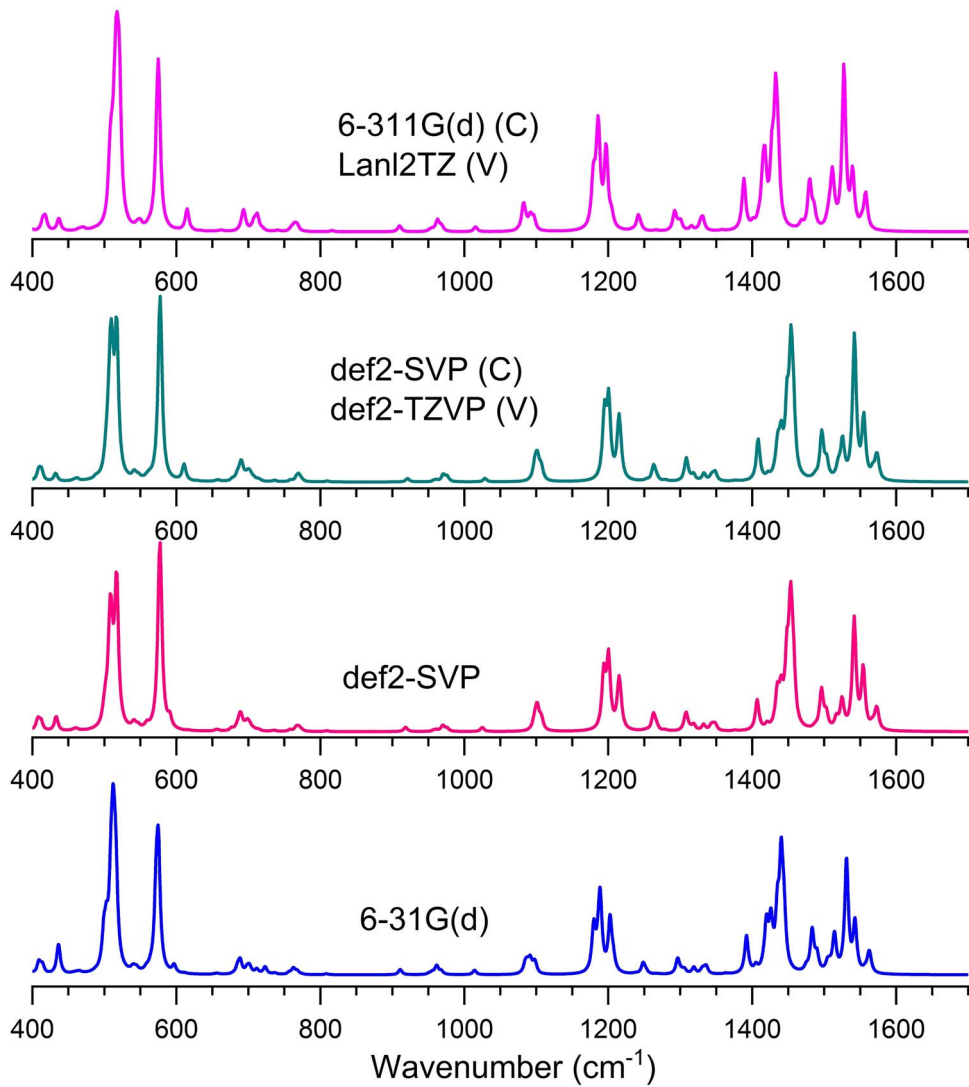


Figure A20. Simulated infrared spectra of the most stable C_{60}V^+ using the BPW91 functional with different basis sets. The spectra are convolved using Lorentzian line shapes of 6 cm^{-1} FWHM. It can be seen that the basis sets have a minor effect on the simulated spectra regarding both the band positions and intensities.

ORCID iDs

Gao-Lei Hou [ID](https://orcid.org/0000-0003-1196-2777) <https://orcid.org/0000-0003-1196-2777>
 Olga V. Lushchikova [ID](https://orcid.org/0000-0002-5699-6818) <https://orcid.org/0000-0002-5699-6818>
 Joost M. Bakker [ID](https://orcid.org/0000-0002-1394-7661) <https://orcid.org/0000-0002-1394-7661>
 Peter Lievens [ID](https://orcid.org/0000-0001-6570-0559) <https://orcid.org/0000-0001-6570-0559>
 Leen Decin [ID](https://orcid.org/0000-0002-5342-8612) <https://orcid.org/0000-0002-5342-8612>
 Ewald Janssens [ID](https://orcid.org/0000-0002-5945-1194) <https://orcid.org/0000-0002-5945-1194>

References

- Bakker, J. M., Lapoutre, V. J. F., Redlich, B., et al. 2010, *JChPh*, **132**, 074305
 Baluteau, J.-P., Zavagno, A., Morisset, C., & Péquignot, D. 1995, *A&A*, **303**, 175
 Berkowitz, J. 1999, *JChPh*, **111**, 1446
 Bernal, J. J., Haenecour, P., Howe, J., et al. 2019, *ApJL*, **883**, L43
 Bernard-Salas, J., Cami, J., Peeters, E., et al. 2012, *ApJ*, **757**, 41
 Berné, O., Cox, N. L. J., Mulas, G., & Joblin, C. 2017, *A&A*, **605**, L1
 Berné, O., Montillaud, J., & Joblin, C. 2015, *A&A*, **577**, A133
 Berné, O., Mulas, G., & Joblin, C. 2013, *A&A*, **550**, L4
 Boersma, C., Bauschlicher, C. W. Jr., Ricca, A., et al. 2014, *ApJS*, **211**, 8
 Brieva, A. C., Gredel, R., Jäger, C., Huisken, F., & Henning, T. 2016, *ApJ*, **826**, 122
 Calvo, F., Li, Y., Kiawi, D. M., et al. 2015, *PCCP*, **17**, 25956
 Cami, J., Bernard-Salas, J., Peeters, E., & Malek, S. E. 2010, *Sci*, **329**, 1180
 Cami, J., Bernard-Salas, J., Peeters, E., & Malek, S. E. 2011, in IAU Symp. 280, The Molecular Universe, ed. J. Cernicharo & R. Bachiller (Cambridge: Cambridge Univ. Press), **216**
 Campbell, E. K., Holz, M., Gerlich, D., & Maier, J. P. 2015, *Natur*, **523**, 322
 Candan, A., Zhen, J., & Tielens, A. G. G. M. 2018, *PhT*, **71**, 38
 Castellanos, P., Berné, O., Sheffer, Y., Wolfire, M. G., & Tielens, A. G. G. M. 2014, *ApJ*, **794**, 83
 Cordiner, M. A., Linnartz, H., Cox, N. L. J., et al. 2019, *ApJL*, **875**, L28
 Dunk, P. W., Adjizian, J. -J., Kaiser, N. K., et al. 2013, *PNAS*, **110**, 18081
 Dunk, P. W., Mulet-Gas, M., Nakanishi, Y., et al. 2014, *NatCo*, **5**, 5844
 Esconjauregui, S., Whelan, C. M., & Maex, K. 2009, *Carbon*, **47**, 659
 Ferrari, P., Janssens, E., Lievens, P., & Hansen, K. 2019, *IRPC*, **38**, 405
 Ferrari, P., Vanbuel, J., Li, Y., et al. 2017, in Gas-Phase Synthesis of Nanoparticles, ed. Y. Huttel (Weinheim: Wiley-VCH), 59
 Foing, B. H., & Ehrenfreund, P. 1994, *Natur*, **369**, 296
 Frisch, M. J., Trucks, G. W., Schlegel, H. B., et al. 2013, Gaussian 09, Revision E.01, Gaussian, Inc., Wallingford CT, <https://gaussian.com/>
 García-Hernández, D. A., Manchado, A., García-Lario, P., et al. 2010, *ApJL*, **724**, L39
 García-Hernández, D. A., Iglesias-Groth, S., Acosta-Pulido, J. A., et al. 2011, *ApJL*, **737**, L30
 Hoeijmakers, H. J., Ehrenreich, D., Hend, K., et al. 2018, *Natur*, **560**, 453
 Hoeijmakers, H. J., Ehrenreich, D., Kitzmann, D., et al. 2019, *A&A*, **627**, A165
 Hou, G.-L., Yang, T., Li, M., et al. 2021, *AngCh*, **60**, 27095
 Iglesias-Groth, S., & Esposito, M. 2013, *ApJL*, **776**, L2

- Jacquemin, D., Perpète, E. A., Scuseria, G. E., Ciofini, I., & Adamo, C. 2007, *JCTC*, 4, 123
- Jenkins, E. B. 2009, *ApJ*, 700, 1299
- Kaminski, T., Mason, E., Tylenda, R., & Schmidt, M. R. 2015, *A&A*, 580, A34
- Klots, C. E. 1991, *ZPhyD*, 21, 335
- Knacke, R. F. 1977, *Natur*, 269, 132
- Koenig, J. L. 1999, Spectroscopy of Polymers (2nd edn.; Amsterdam: Elsevier), 77
- Krätschmer, W., Lamb, Lowell D., Fostiropoulos, K., & Huffman, Donald R. 1990, *Natur*, 347, 354
- Kroto, H. W. 1988, *Sci*, 242, 1139
- Kroto, H. W., Heath, J. R., O'Brien, S. C., Curl, R. F., & Smalley, R. E. 1985, *Natur*, 318, 162
- Kroto, H. W., & Jura, M. 1992, *A&A*, 263, 275
- Kwok, S. 2017, *NatAs*, 1, 642
- Kwok, S. 2022, *Ap&SS*, 367, 16
- Kwok, S., Volk, K., & Bernath, P. 2001, *ApJL*, 554, L87
- Kwok, S., & Zhang, Y. 2011, *Natur*, 479, 80
- Kwok, S., & Zhang, Y. 2013, *ApJ*, 771, 5
- Laury, M. L., Carlson, M. J., & Wilson, A. K. 2012, *JCoCh*, 33, 2380
- Leger, A., & Puget, J. L. 1984, *A&A*, 137, L5
- Li, A., & Draine, B. T. 2012, *ApJL*, 760, L35
- Li, M., Yang, T., Bakker, J. M., Janssens, E., & Hou, G.-L. 2022, *CRPS*, 3, 100910
- Lykhin, A. O., Ahmadvand, S., & Varganov, S. A. 2018, *JPCL*, 10, 115
- Maier, J. P., & Campbell, E. K. 2017, *AngCh*, 56, 4920
- Micelotta, E. R., Jones, A. P., & Tielens, A. G. G. M. 2010, *A&A*, 510, A36
- Milanova, Y. V., & Kholygin, A. F. 2009, *AstL*, 35, 518
- Nemes, Laszlo, Ram, Ram S., Bernath, Peter F., et al. 1994, *CPL*, 218, 295
- Omont, A. 2016, *A&A*, 590, A52
- Otsuka, M., Kemper, F., Leal-Ferreira, M. L., et al. 2016, *MNRAS*, 462, 12
- Palotás, J., Martens, J., Berden, G., & Oomens, J. 2020, *NatAs*, 4, 240
- Planck Collaboration, Ade, P. A. R., Aghanim, N., et al. 2016, *A&A*, 594, A13
- Pogulay, A. V., Abzalimov, R. R., Nasibullaev, S. K., et al. 2004, *IJMSp*, 233, 165
- Roithová, J., Gray, A., Andris, E., Jaščík, J., & Gerlich, D. 2016, *Acc. Chem. Res.*, 49, 223
- Russell, R. W., Soifer, B. T., & Willner, S. P. 1977, *ApJL*, 217, L149
- Salama, F. 2008, in IAU Symp. 251, Organic Matter in Space (Cambridge: Cambridge Univ. Press), 357
- Savage, Blair D., & Sembach, Kenneth R. 1996, *ARA&A*, 34, 279
- Schlarmann, L., Foing, B., Cami, J., & Fan, H. 2021, *A&A*, 656, L17
- Schwerdtfeger, P., & Nagle, J. K. 2019, *MolPhys*, 117, 1200
- Sellgren, K., Werner, M. W., Ingalls, J. G., et al. 2010, *ApJL*, 722, L54
- Soler, J., Sarkar, R., & Boggio-Pasqua, M. 2019, *JPCA*, 123, 1824
- Tielens, A. G. G. M. 2005, The Physics and Chemistry of the Interstellar Medium (Cambridge: Cambridge Univ. Press)
- Tielens, A. G. G. M. 2008, *ARA&A*, 46, 289
- Tielens, A. G. G. M. 2013, *RvMP*, 85, 1021
- Tomita, S., Andersen, J. U., Hansen, K., & Hvelplund, P. 2003, *CPL*, 382, 120
- Waelkens, C., Van Winckel, H., Trams, N. R., & Waters, L. B. F. M. 1992, *A&A*, 256, L15
- Woods, P. 2020, *NatAs*, 4, 299
- Yanai, T., Tew, D. P., & Handy, N. C. 2004, *CPL*, 393, 51
- Yang, N., Duong, C. H., Kelleher, P. J., McCoy, A. B., & Johnson, M. A. 2019, *Sci*, 364, 275
- Yuan, J., Wang, P., Hou, G.-L., et al. 2016, *JPCA*, 120, 1520
- Zhang, Y., & Kwok, S. 2013, *EP&S*, 65, 1069
- Zhang, Y., Sadjadi, S., Hsia, C.-H., & Kwok, S. 2017, *ApJ*, 845, 76